Commun. Comput. Phys.
doi: 10.4208/cicp.OA-2025-0009

Vol. **39**, No. 1, pp. 185-214
January 2026

Computational Method of Grain Boundary Energy Consistent for Different Orientations and Applications to Double Gyroid Beyond Twinning

Jing Chen[1], Kai Jiang[1,*] Zhangpeng Sun[1] and Jie Xu[2,*]

[1] *Hunan Key Laboratory for Computation and Simulation in Science and Engineering, Key Laboratory of Intelligent Computing and Information Processing of Ministry of Education, School of Mathematics and Computational Science, Xiangtan University, Xiangtan, Hunan, China, 411105.*
[2] *SKLMS & NCMIS, Institute of Computational Mathematics and Scientific/Engineering Computing (ICMSEC), Academy of Mathematics and Systems Science (AMSS), Chinese Academy of Sciences, Beijing, China.*

Received 9 January 2025; Accepted (in revised version) 20 May 2025

Abstract. We develop the method for computing grain boundary (GB) energy consistent for different grain orientations for phase-field type models. The computation is carried out in a parallelepiped domain such that public periodicity is attained along two edges parallel to the dividing plane of two grains. The width of the normal direction is carefully chosen such that the part of each grain in the computational domain can be reassembled into several unit cells. In this way, the bulk energy per volume in the computational domain is identical to the energy density of a unit cell, so that GB energy of different orientations can be obtained in a unified standard. We apply this method to the study of four double-gyroid (DG) GBs with different orientations numerically using the Landau–Brazovskii free energy, including the (422) twin boundary studied recently, a network switching GB, and two tilt GBs. Topological variations and geometric deformations are investigated. It is found that deviations in strut lengths and dihedral angles from the bulk DG substantially exceed changes in strut angles and nodal coplanarity. We also examine the spectra along the contact plane of two grains and utilize them to evaluate the GB widths. Of the four GBs we study, the network switching GB changes to the least extent topologically and geometrically, meanwhile has the lowest energy and the smallest GB width.

AMS subject classifications: 35Q82, 35J35, 35J40, 65N35, 82B24, 74E15

Key words: Grain boundary energy, orientation, phase-field model, double gyroid, network switching.

---

[*]Corresponding author. *Email addresses:* `kaijiang@xtu.edu.cn` (K. Jiang), `xujie@lsec.cc.ac.cn` (J. Xu)

1 Introduction

The double gyroid (DG) has been observed in various materials, including block copolymers [1–4], liquid crystal polymers [5, 6], lipid mesophases [7, 8], surfactants [9–11], and biological assemblies [12–14]. The ideal DG skeleton has two interpenetrating networks with opposite chirality [15,16], typically given by the higher-concentration region of a component. Each network is featured by three coplanar struts of equal length from each node to three adjacent ones with the angle 120°. Such planes rotate $\pm\arccos(1/3)$ ($\approx\pm 70.5^\circ$) along the clockwise($+$)/counterclockwise($-$) network, generating the shortest ten-node circuits [17] and the unit cell of the $Ia\bar{3}d$ space group. The particular symmetries and skeletons lead to unique properties, including excellent mechanical [18–23], optical [14,24,25], mass transport properties [26,27] and highly uniform porousness [28,29]. These properties may be affected by defect structures [30] that are yet well-understood.

Defects in network structures involve changes of graph topology and geometry [17,18,31–36], thus are more complicated. For DG, a well-structured (422) ‡ twin boundary (TB) with mirror symmetry, possibly first noticed in Ref. [37], has been analyzed in several recent works. This specific structure is examined by minimal surface [38, 39], followed by experiments [39, 40]. Specifically, the fusions of nodes on the TB plane and the resulting alterations of circuits are examined. To coordinate with the TB nodes, the network structure adjacent to these nodes, such as the changes of strut lengths and dihedral angles, undergoes complex deformation. TBs are generally regarded to have lower energy because of their better symmetries, which is suggested by the results of spherical structures [41–44]. However, for DG and other network structures, it requires further studies on GBs of other orientations to validate. Furthermore, it is intriguing to explore whether some mechanisms on the formation of the (422) TB also feature other GBs. To our knowledge, the above problem is yet to be covered experimentally, so we believe that it would be interesting if predictions can be made from the computational aspect.

To comprehend properties of GBs formed by DG or other network structures, it is crucial to examine their morphologies from the energy viewpoint. It thus calls for reliable and efficient computations of the GB energy. Conceptually, GB energy is the excess energy over the bulk energy in the GB system. Since the GB energy relies on the orientations of grains, the definition of the GB energy shall follow a consistent standard in order to be comparable for different orientations. A naive approach is to compute in a periodic domain that matches the period of each grain with the prescribed orientation [45], with each grain occupying half of the computational domain. In this case, the bulk energy per volume in this domain is identical to that of a unit cell. This setting actually studies the system with infinite many GBs in presence periodically, which may affect one another. Meanwhile, the requirement on the periodic domain could make it very large, leading to high computational costs. Another choice is to formulate the GB system in a bounded domain [42, 46]. This approach is more flexible on the computational domain since one

---

‡Miller indices

is not obliged to simultaneously fit two rotated grains in a large unit cell. However, if the domain or the boundary conditions are not carefully chosen, inconsistencies could be introduced. In particular, when the calculation of GB energy is necessary, the bulk energy per volume in the computational domain, as a benchmark, generally *is not* equal to the energy density of the unit cell, which, to our knowledge, is not addressed in previous works. As a result, simply using the bulk energy of a unit cell to calculate the bulk energy in the computational domain will lead to distinction in benchmark for different orientations, causing errors in the calculation of GB energy. Moreover, such errors cannot be reduced when we enlarge the computational domain, as we will discuss in the next section.

In this work, we develop a method for the calculation of GB energy for modulated phases, reliable and comparable for different orientations, which will be described in Section 2. The method is built on the framework established in Ref. [46]. To briefly describe the framework, the GB structure is computed in a banded region between two parallel planes. The two grains with specific orientations are anchored outside, giving the boundary conditions on the two planes. For the GBs we consider in this work, the two grains have common period parallel to the plane, so that a parallelogram unit cell along the plane is available. The free energy is then minimized in a parallelepiped to obtain the optimal GB profile. The numerical approach is established recently with high accuracy [47] that is adequately precise to resolve general anchoring orientations [48]. Here, we further develop the method by choosing appropriate widths of the banded region for the GB energy. Specifically, we show that, when each of the two bounding planes contains a lattice point of the corresponding grain, the part of each grain within the computational domain can be reassembled into several unit cells. Thus, it is straightforward to use the bulk energy of a unit cell to obtain the bulk energy in the computational domain. This approach does not require periodicity in the direction perpendicular to the GB plane, and genuinely computes a single GB instead of infinite many GBs appearing periodically. In this way, we are able to achieve a consistent standard for different orientations of grains.

We utilize this approach to investigate the skeleton of the network using an isosurface of the GB profile, illustrated in Section 3. We adopt the Landau–Brazovskii free energy that can describe many modulated phases including DG [49–52]. The (422) TB presented has the same topology with the experimental result in Ref. [40] and some differences in geometry. More interestingly, we find that a network-switching (NetSw) GB turns out to have lower energy than TB, where one network is connected directly to the other with reversed chirality by struts. We also examine a $[\bar{1}00]$ tilt GB (Tlt1) and a $[\bar{1}10]$ tilt GB (Tlt2), both with higher energy, where new nodes, curved struts are found and larger deformations are observed. The deformation caused by GB is classified into four types: the differences of strut lengths, strut angles, dihedral angles from the bulk DG values, and the coplanarity of a node and its three adjacent ones. The deformations in the two tilt GBs are indeed larger than those in the TB and the NetSw GB. The TB exhibits larger deformations on the contact plane, which may result in a higher energy than the NetSw GB. Apart from the skeleton network, we also investigate the 2D spectra along the contact plane of the GBs that can be naturally extracted from the Fourier expansion. By looking into the spectra with higher intensities, we can more effectively characterize the GB's constituents and more precisely define the GB widths, as previously suggested [48]. Among the four GBs, the NetSw GB turns out to have the fewest number of spectra over certain intensity and the smallest width, which also suggests its lower energy. Concluding remarks are given in Section 4.

2 Methods

Since many notations will be introduced below, we summarize these notations in Table 1 for the convenience of readers.

We use the Landau–Brazovskii (LB) model of a scalar order parameter ϕ, which can describe typical modulated phases including DG. The free energy per volume, in a dimensionless form, is given by [49–51]

$$E(\phi(\mathbf{r});\Omega)=\frac{1}{V(\Omega)}\int_{\Omega}f(\phi,\nabla\phi,\nabla^2\phi)\mathrm{d}\mathbf{r} \tag{2.1}$$

with

$$f(\phi,\nabla\phi,\nabla^2\phi)=\frac{1}{2}[(\Delta+1)\phi(\mathbf{r})]^2+\frac{\tau}{2}[\phi(\mathbf{r})]^2-\frac{\gamma}{3!}[\phi(\mathbf{r})]^3+\frac{1}{4!}[\phi(\mathbf{r})]^4, \tag{2.2}$$

where $\mathbf{r}=(x,y,z)^T$, $V(\Omega)$ is the volume of the region Ω, and the coefficients τ, γ, depending on the material, may relate to various physical parameters [53, 54]. The total mass $\bar{\phi}=(1/V(\Omega))\int_{\Omega}\phi(\mathbf{r})\mathrm{d}\mathbf{r}$ is required to be conserved.

A periodic bulk phase can be represented by a Fourier series,

$$\phi_0(\boldsymbol{r})=\sum_{\boldsymbol{k}\in\mathbb{Z}^3}\hat{\phi}_0(\boldsymbol{k})e^{i(\mathcal{P}\boldsymbol{k})^T\boldsymbol{r}}. \tag{2.3}$$

Its profile is obtained by minimizing the LB free energy in a parallelepiped unit cell, meanwhile optimizing the cell parameters $\mathcal{P}$ [52, 55, 56]. It follows that the columns of $\mathcal{W}=2\pi\mathcal{P}^{-1}\triangleq(\boldsymbol{w}_1,\boldsymbol{w}_2,\boldsymbol{w}_3)$ give the edges of a unit cell $\mathscr{W}$.

Table 1: Summary of key notations.

Notation	Description
$\mathscr{W}$	Parallelepiped unit cell
$\boldsymbol{w}_1,\boldsymbol{w}_2,\boldsymbol{w}_3$	Basis vectors of parallelepiped $\mathscr{W}$
$\mathscr{D}$	Parallelogram defining common periodicity in the y-z plane
$\boldsymbol{u}_1,\boldsymbol{u}_2$	Basis vectors of Parallelogram $\mathscr{D}$
$E_{\text{bulk},1},E_{\text{bulk},2}$	Bulk energy densities for grain 1 and grain 2
E_0	Energy density for the unit cell

A GB is formed by two grains of a phase with different orientations. To formulate the GB system, we pose the two grains with certain orientations, in the half spaces $x<0$ and $x>0$, respectively. We introduce two rotation matrices $R_s \in SO(3)$ to express the orientations of two grains, where $s=1,2$ represents the grains in $x<0$ and $x>0$, respectively. We further write out for R_s the first and the other two columns as $R_s=(R_{sx},\tilde{R}_s)$. The profiles of two rotated grains are then written as

$$\phi_s(\boldsymbol{r})=\phi_0(R_s\boldsymbol{r})=\sum_{\boldsymbol{k}\in\mathbb{Z}^3}\hat{\phi}_0(\boldsymbol{k})e^{i\left(R_{sx}^T\mathcal{P}\boldsymbol{k}\right)x}e^{i\left(\tilde{R}_s^T\mathcal{P}\boldsymbol{k}\right)^T\tilde{\boldsymbol{r}}}, \tag{2.4}$$

where $\tilde{\boldsymbol{r}}=(y,z)^T$. Define $\tilde{\mathcal{P}}_s=\tilde{R}_s^T\mathcal{P}\in\mathbb{R}^{2\times3}$, $\hat{\phi}_s(x,\boldsymbol{k})=\hat{\phi}_0(\boldsymbol{k})e^{i\left(R_{sx}^T\mathcal{P}\boldsymbol{k}\right)x}$. In this work, we focus on special cases that two grains have common period in the y-z plane, and use 2D Fourier expansion according to a parallelogram $\mathscr{D}$ giving a periodicity of the grains. The 2D Fourier expansion can also be constructed by extracting (two) linearly independent column vectors from the 2×6 matrix $(\tilde{\mathcal{P}}_1,\tilde{\mathcal{P}}_2)$, denoted as $\tilde{\mathcal{P}}$ that is 2×2. Similar to the bulk phase, the edges of $\mathscr{D}$ is given by $\mathcal{D}=2\pi\tilde{\mathcal{P}}^{-1}$. In the x-direction, we choose some L_1 and L_2 adequately containing the GB transition region and let GB relax in $-L_1\leq x\leq L_2$. The GB system has been formulated in detail in [46], for which we write down the essentials below. The GB structure is a local minimizer of the free energy (2.1), typically obtained by evolving the gradient flow,

$$\frac{\partial\phi}{\partial t}=-\left(\nabla^2+1\right)^2\phi-\left(\tau\phi-\frac{\gamma}{2}\phi^2+\frac{1}{6}\phi^3\right)-\xi, \tag{2.5}$$

where a Lagrange multiplier ξ is determined by the mass conservation. The initial state can be constructed by simply connecting the two grains ϕ_1 and ϕ_2, i.e.,

$$\phi^{(0)}(x,\tilde{\boldsymbol{r}})=\sum_{\boldsymbol{k}\in\mathbb{Z}^2}\left[(1-b(x))\hat{\phi}_1(x,\boldsymbol{k})+b(x)\hat{\phi}_2(x,\boldsymbol{k})\right]e^{i\left(\tilde{\mathcal{P}}\boldsymbol{k}\right)^T\tilde{\boldsymbol{r}}}, \tag{2.6}$$

where $b(x)=[1-\tanh(\sigma x)]/2$ with a large σ, satisfying that $b(-L_1)=0$ and $b(L_2)=1$. The anchoring boundary conditions are given by the function value and its normal derivative at $x=-L_1$ and $x=L_2$, which are set equal to the rotated bulk values $\phi_s(\boldsymbol{r})$ of two grains, i.e.,

$$\left.\frac{\partial^m\phi(x,\tilde{\boldsymbol{r}})}{\partial x^m}\right|_{x=-L_1}=\left.\frac{\partial^m\phi_1(x,\tilde{\boldsymbol{r}})}{\partial x^m}\right|_{x=-L_1},\quad\left.\frac{\partial^m\phi(x,\tilde{\boldsymbol{r}})}{\partial x^m}\right|_{x=L_2}=\left.\frac{\partial^m\phi_2(x,\tilde{\boldsymbol{r}})}{\partial x^m}\right|_{x=L_2}, \tag{2.7}$$

where $m=0,1$. We shall emphasize that the boundary conditions at $x=-L_1$, $x=L_2$ and the choice of $\tilde{\mathcal{P}}$ depend on the posing of the two grains. The discretization in the x-direction is implemented by generalized Jacobi polynomial that ensures sufficient accuracy [47]. The method to evolve the gradient flow is identical to the previous works, which may include some modifications to accelerate [46–48]. Details of this numerical implementation are discussed in preceding works [47,48].

As previously discussed [46, 57], for modulated phases, a GB system, or more generally an interface system, generally has multiple local minimizers. Different local minimizers represent GB or interfaces at different locations that can be visibly distinguished from one another, which we have verified for the GBs we discuss in this work. What we focus on is the GB located at $x=0$.

Now let us turn to the calculation of GB energy. In the above setting, we are devoted to minimizing the total energy of the GB system, which contains both the bulk energy and the GB energy. Indeed, if one only cares about a single GB with certain grain orientations, such an energy minimization reaches the optimally relaxed structure. Nonetheless, it is crucial to comprehend the relations of GBs of different orientations, which calls for extracting the GB energy from the total energy. The notion of interfacial energy, GB energy as its special case, originates from spatially homogeneous phases, defined as excess energy over the bulk energy. Straightforwardly, the bulk energy for spatially homogeneous phases is proportional to the volume. But it is not the case for modulated phases, because the part of each grain within the computational domain may not consist of whole unit cells. When this is the case, the energy of this part deviates from the energy density of the unit cell, denoted as E_0, multiplied by the volume of the grain within the computational domain. For this reason, we cannot use the bulk energy density directly in the calculation of GB energy. Actually, such a deviation introduces an error that does not decay when we enlarge the computational domain. Since we pose the two grains in $x\in[-L_1,0]$ and $x\in[0,L_2]$, the bulk energy for grain 1 shall be given by

$$E_{\text{bulk},1}(L_1,\mathscr{D})=\frac{1}{L_1S(\mathscr{D})}\int_{[-L_1,0]\times\mathscr{D}}f(\phi_1,\nabla\phi_1,\nabla^2\phi_1)\mathrm{d}\boldsymbol{r}. \tag{2.8}$$

Similarly $E_{\text{bulk},2}(L_2,\mathscr{D})$ can be defined. The fact that the bulk phase is modulated implies that $E_{\text{bulk},1}$ oscillates with L_1 around E_0. It is seemingly not a problem since $E_{\text{bulk},1}\to E_0$ when $L_1\to\infty$. However, we could realize that the oscillation leads to non-decaying deviation. In fact, the GB energy per area, shall then be defined as

$$\delta_{\text{GB}}=(L_1+L_2)E(\phi;[-L_1,L_2]\times\mathscr{D})-L_1E_{\text{bulk},1}-L_2E_{\text{bulk},2}, \tag{2.9}$$

where the factor L_1^{-1} that drives $E_{\text{bulk},1}\to E_0$ is cancelled. The difference turns out to be $L_1(E_{\text{bulk},1}(L_1,\mathscr{D})-E_0)$ that does not diminish when enlarging L_1, illustrated in Fig. 1 where we compute $L_1(E_{\text{bulk},1}-E_0)$. More generally, the above analysis indicates that the scaling of the part of grains that does not compose whole unit cells is the same as the GB area. Therefore, similar issue is present when using other finite-domain settings, which we would not run into details since it goes beyond the main topic of this work.

To resolve this issue, one option is to calculate $E_{\text{bulk},i}(L_i,\mathscr{D})$ for the chosen L_i for i=1,2. This approach requires solving one minimization problem for each of the two grains, at a cost comparable with solving the GB system, with its prescribed orientation, L_i, and corresponding boundary conditions. As a result, it is computationally expensive and introduces errors due to discretization. Here, our solution is delicate choice of L_1 (resp.

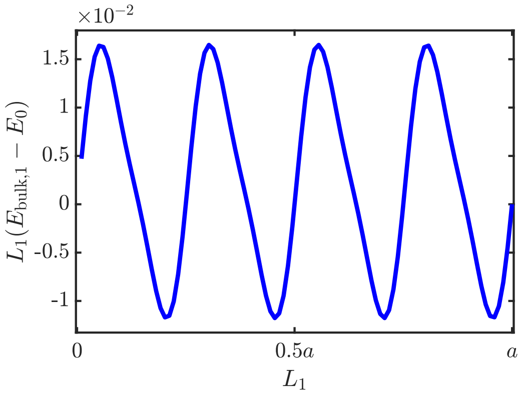

Figure 1: The bulk energy $E_{\text{bulk},1}$ (see (2.8) for the definition) of a (422) grain oscillates with L_1. Here, a denotes the edge length of the bulk DG unit cell.

L_2) such that the part of bulk phase lying within $[-L_1,0]\times\mathscr{D}$ (resp. $[0,L_2]\times\mathscr{D}$) can be reassembled into several unit cells. In this case, we will have $E_{\text{bulk},1}(L_1,\mathscr{D})=E_0$ so that the bulk energy density can be used. It shall be noted that those L_1 satisfying the above condition are not restrained to those making the x-direction periodic, which we shall recognize below. Therefore, it gives much more flexibility in the computational domain.

In the following, we shall focus on the part of the bulk phase within $[-L_1,0]$ and $[0,L_2]$, and only discuss grain 2, i.e. $\phi_2(\boldsymbol{r})$ within $[0,L_2]$, because similar arguments hold for grain 1. Our discussion will be carried out with the coordinates in the bases given by the unit cell $\mathscr{W}=(\boldsymbol{w}_1,\boldsymbol{w}_2,\boldsymbol{w}_3)$, denoted as (s_1,s_2,s_3). By the definition, lattice points of the bulk phase are located at $s_i\in\mathbb{Z}$. The plane $x=0$ is then written as $as_1+bs_2+cs_3=0$. Here, we assume that the plane passes the origin, denoted as O, without loss of generality, since otherwise we can impose a translation on the lattice. Moreover, since periodicity has been demanded in the y-z plane, the coefficients can be taken as $a,b,c\in\mathbb{Z}$, which is a direction result from the fact that the plane contains two linearly independent (s_1,s_2,s_3) where $s_i\in\mathbb{Z}$.

Let us recall the summation of two sets, defined as

$$\mathscr{A}+\mathscr{B}=\{\boldsymbol{a}+\boldsymbol{b}:\boldsymbol{a}\in\mathscr{A},\,\boldsymbol{b}\in\mathscr{B}\}.$$

It is a convenient way to express a parallelogram or parallelepiped.

Since the bulk phase is periodic, any translation along the lattice vectors leaves the structural configuration invariant. Let us define an equivalence for this.

Definition 2.1. Let $\mathscr{A}$ and $\mathscr{B}$ be two regions within a periodic bulk structure. They are said to be equivalent, denoted as $\mathscr{A}\sim\mathscr{B}$, if $\mathscr{B}=\mathscr{A}+\boldsymbol{v}$ for any lattice vector $\boldsymbol{v}$, i.e. $\boldsymbol{v}=z_1\boldsymbol{w}_1+z_2\boldsymbol{w}_2+z_3\boldsymbol{w}_3$ for any $z_1,z_2,z_3\in\mathbb{Z}$, where $\boldsymbol{w}_i$ are the lattice vectors.

Furthermore, the equivalence can be extended if two regions can be divided into parts such that these parts are correspondingly equivalent.

Definition 2.2. If $\mathscr{A}=\cup_{i=1}^{K}\mathscr{A}_i$, $\mathscr{B}=\cup_{i=1}^{K}\mathscr{B}_i$ where $\mathscr{A}_i\cap\mathscr{A}_j$, $\mathscr{B}_i\cap\mathscr{B}_j$ are volume-zero and $\mathscr{B}_i=\mathscr{A}_i+\boldsymbol{v}_i$ where $\boldsymbol{v}_i$ are lattice vectors for $i=1,\cdots,K$, then $\mathscr{A}\sim\mathscr{B}$.

It is clear that Definition 2.1 is a special case of Definition 2.2. Moreover, the equivalence relation is transitive.

Proposition 2.1. If $\mathscr{A}\sim\mathscr{B}$, $\mathscr{B}\sim\mathscr{C}$, then $\mathscr{A}\sim\mathscr{C}$.

Proof. Let us write $\mathscr{A}=\cup_{i=1}^{K}\mathscr{A}_i$, $\mathscr{B}=\cup_{i=1}^{K}\mathscr{B}_i$, such that $\mathscr{A}_i\cap\mathscr{A}_j$, $\mathscr{B}_i\cap\mathscr{B}_j$ are volume-zero and $\mathscr{B}_i=\mathscr{A}_i+\boldsymbol{v}_i$ where $\boldsymbol{v}_i$ are lattice vectors for $i=1,\cdots,K$. Also, let us write $\mathscr{B}=\cup_{i=1}^{K'}\mathscr{B}'_i$, $\mathscr{C}=\cup_{i=1}^{K'}\mathscr{C}'_i$, such that $\mathscr{B}'_i\cap\mathscr{B}'_j$, $\mathscr{C}'_i\cap\mathscr{C}'_j$ are volume-zero and $\mathscr{C}'_i=\mathscr{B}'_i+\boldsymbol{v}'_i$ where $\boldsymbol{v}'_i$ are lattice vectors for $i=1,\cdots,K'$. Notice that $\mathscr{B}=\cup_{1\le i\le K,1\le j\le K'}\mathscr{B}_i\cap\mathscr{B}'_j$, where $(\mathscr{B}_{i_1}\cap\mathscr{B}'_{j_1})\cap(\mathscr{B}_{i_2}\cap\mathscr{B}'_{j_2})$ are volume-zero. As a result,

$$\begin{aligned}\mathscr{A}_i&=\mathscr{B}_i-\boldsymbol{v}_i=\cup_{j=1}^{K'}(\mathscr{B}_i\cap\mathscr{B}'_j-\boldsymbol{v}_i)\\&=\cup_{j=1}^{K'}((\mathscr{B}_i-\boldsymbol{v}_i)\cap(\mathscr{B}'_j-\boldsymbol{v}_i))=\cup_{j=1}^{K'}(\mathscr{A}_i\cap(\mathscr{B}'_j-\boldsymbol{v}_i)),\end{aligned}$$

followed by

$$\mathscr{A}=\cup_{i=1}^{K}\mathscr{A}_i=\cup_{1\le i\le K,1\le j\le K'}(\mathscr{A}_i\cap(\mathscr{B}'_j-\boldsymbol{v}_i)),$$

where the intersection of any two terms in the union $\cup_{1\le i\le K,1\le j\le K'}$ above is volume-zero. Similarly, we can write

$$\begin{aligned}&\mathscr{C}'_j=\mathscr{B}'_j+\boldsymbol{v}'_j=\cup_{i=1}^{K}(\mathscr{B}'_j\cap\mathscr{B}_i+\boldsymbol{v}'_j)=\cup_{i=1}^{K}(\mathscr{C}'_i\cap(\mathscr{B}_i+\boldsymbol{v}_j)).\\&\mathscr{C}=\cup_{1\le i\le K,1\le j\le K'}(\mathscr{C}'_i\cap(\mathscr{B}_i+\boldsymbol{v}_j)).\end{aligned}$$

It remains to notice that

$$(\mathscr{A}_i\cap(\mathscr{B}'_j-\boldsymbol{v}_i))+\boldsymbol{v}_i+\boldsymbol{v}'_j=\mathscr{B}_i\cap\mathscr{B}'_j+\boldsymbol{v}'_j=\mathscr{C}'_i\cap(\mathscr{B}_i+\boldsymbol{v}_j).$$

This completes the proof. □

To express that $[0,L_2]\times\mathscr{D}$ can be reassembled into several unit cells, it requires that $[0,L_2]\times\mathscr{D}=\mathscr{A}\backslash\mathscr{B}$ for two regions $\mathscr{B}\subseteq\mathscr{A}$, such that both $\mathscr{A}$ and $\mathscr{B}$ are equivalent to several whole unit cells.

Notice that the choice of $\mathscr{D}$ is not unique. For the convenience of our discussions, we first show that the choice of $\mathscr{D}$ in the y-z plane makes no difference in the bulk energy per volume $E_{\text{bulk},2}(L_2,\mathscr{D})$. Thus, we could select the most suitable $\mathscr{D}$ for different cases.

Lemma 2.1. *Let $\mathscr{D}$ and $\mathscr{D}'$ both be periodicity of ϕ_2 in the y-z plane. For any L_2, it holds $E_{\text{bulk},2}(L_2,\mathscr{D}')=E_{\text{bulk},2}(L_2,\mathscr{D})$.*

Proof. Here, our focus is on the y-z plane instead of $x=L_2$. We shall show that there exists a smallest parallelogram that gives a periodicity of ϕ_2 in the y-z plane, and utilize this to obtain the equality. First, let us pick up within the plane $x=0$ a point closest to the origin that makes ϕ_2 periodic along the vector from the origin to this point, denoted as $\boldsymbol{u}_1$. We might be unable to do it, since the infimum distance of two distinct points might be zero. But this implies that ϕ_2 is homogeneous in at least one direction within the y-z plane, which reduces to a much simpler case that we omit. Then, outside the line containing the vector $\boldsymbol{u}_1$, let us pick another bulk lattice point in the plane $x=0$ with the smallest distance to the line, and denote by $\boldsymbol{u}_2$ the vector from the origin to this point. Such a selecting procedure implies that no bulk lattice point lies in the parallelogram generated by $\boldsymbol{u}_1$ and $\boldsymbol{u}_2$, otherwise there will be another point with less distance to the line. Consider the lattice generated from $\boldsymbol{u}_1$ and $\boldsymbol{u}_2$ within the plane $x=0$. It follows that any periodic region along the y-z plane is given by two lattice vectors generated from $\boldsymbol{u}_1$ and $\boldsymbol{u}_2$, otherwise it contradicts the above selecting procedure.

Let $\mathscr{D}'$ be another periodicity of ϕ_2 in the y-z plane, generated by two lattice vectors $\boldsymbol{u}_1'$ and $\boldsymbol{u}_2'$, which can be written as integer linear combinations of $\boldsymbol{u}_1$ and $\boldsymbol{u}_2$, i.e.,

$$(\boldsymbol{u}_1',\boldsymbol{u}_2')=(\boldsymbol{u}_1,\boldsymbol{u}_2)\begin{pmatrix} a_{11} & a_{12} \\ a_{21} & a_{22} \end{pmatrix}, \quad a_{ij}\in\mathbb{Z}.$$

We assume without generality that $a_{11},a_{12}\geq 0$, or we could use $-\boldsymbol{u}_1$ to substitute $\boldsymbol{u}_1$.

Case one: $a_{21}a_{22}\geq 0$. We could assume that $a_{21},a_{22}\geq 0$ (otherwise use $-\boldsymbol{u}_2$ to substitute $\boldsymbol{u}_2$), and $a_{11}a_{22}\geq a_{21}a_{12}$ (otherwise switch $\boldsymbol{u}_1'$ and $\boldsymbol{u}_2'$) (see Fig. 2 (a)). Consider a larger parallelogram OA_3CB_3, with the points given by

$$\begin{aligned}
&\overrightarrow{OA}=\boldsymbol{u}_1', \quad \overrightarrow{OB}=\boldsymbol{u}_2', \quad \overrightarrow{OC}=\boldsymbol{u}_1'+\boldsymbol{u}_2', \\
&\overrightarrow{OA_1}=a_{11}\boldsymbol{u}_1, \quad \overrightarrow{OA_2}=\boldsymbol{u}_1'+a_{12}\boldsymbol{u}_1, \quad \overrightarrow{OA_3}=(a_{11}+a_{12})\boldsymbol{u}_1 \\
&\overrightarrow{OB_1}=a_{22}\boldsymbol{u}_2, \quad \overrightarrow{OB_2}=\boldsymbol{u}_2'+a_{21}\boldsymbol{u}_2, \quad \overrightarrow{OB_3}=(a_{21}+a_{22})\boldsymbol{u}_2.
\end{aligned}$$

Since a_{ij} are integers, the parallelograms OA_3CB_3, $AA_1A_3A_2$, $BB_1B_3B_2$ are formed by several unit cells. For the four triangles, it follows that $\triangle OAA_1\cup\triangle BB_2C\sim\{\lambda_1a_{11}\boldsymbol{u}_1+\lambda_2a_{21}\boldsymbol{u}_2:0\leq\lambda_{1,2}\leq 1\}$ and $\triangle OBB_1\cup\triangle AA_2C\sim\{\lambda_1a_{12}\boldsymbol{u}_1+\lambda_2a_{22}\boldsymbol{u}_2:0\leq\lambda_{1,2}\leq 1\}$. In other words, let $\mathscr{A}$ be the parallelogram OA_3CB_3, $\mathscr{B}$ is the union of four triangles and two small parallelograms. Then $\mathscr{D}'=\mathscr{A}\backslash\mathscr{B}$, where $\mathscr{B}\subseteq\mathscr{A}$, and both $\mathscr{A}$ and $\mathscr{B}$ are equivalent to several whole unit cells.

Case two: $a_{21}a_{22}<0$. As above, we could assume $a_{21}<0$, $a_{22}>0$ (Fig. 2 (b)). Also consider a larger parallelogram $A_1B_1C_2C_1$, with the points given by

$$\begin{aligned}
&\overrightarrow{OA}=\boldsymbol{u}_1', \quad \overrightarrow{OB}=\boldsymbol{u}_2', \quad \overrightarrow{OC}=\boldsymbol{u}_1'+\boldsymbol{u}_2', \\
&\overrightarrow{OA_1}=a_{21}\boldsymbol{u}_2, \quad \overrightarrow{OB_1}=a_{22}\boldsymbol{u}_2, \quad \overrightarrow{OC_1}=\boldsymbol{u}_1'+a_{12}\boldsymbol{u}_1, \quad \overrightarrow{OC_2}=\boldsymbol{u}_2'+a_{11}\boldsymbol{u}_1.
\end{aligned}$$

Then $\mathscr{D}'=\mathscr{A}\backslash\mathscr{B}$, where $\mathscr{A}$ is the parallelogram $A_1B_1C_2C_1$, and $\mathscr{B}$ is the union of four triangles. Similar arguments can be drawn as case one. □

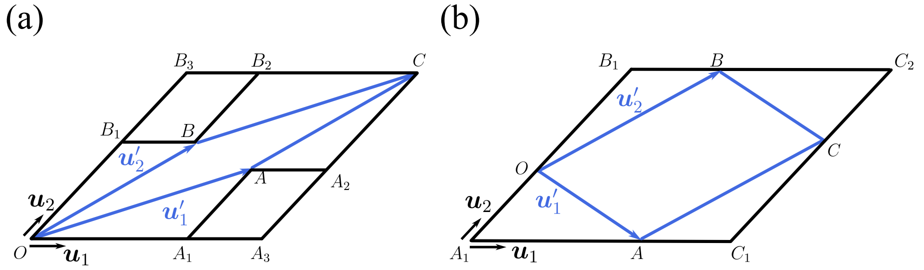

Figure 2: Two cases in Lemma 2.1. (a) $a_{21},a_{22}\geq 0$ and $a_{11}a_{22}\geq a_{21}a_{12}$. (b) $a_{21}<0$, $a_{22}>0$.

In the following, we shall use the notation $\mathscr{D}$ to represent a parallelogram, which is convenient for our discussion, representing the periodicity in the y-z plane. Next, we show that a shear along a direction in the y-z plane leads to equivalence.

Lemma 2.2. *For any two points E and E' lying within the plane $x=L_2$, it holds that*

$$\mathscr{D}+\{\lambda\overrightarrow{OE}:\lambda\in[0,1]\}\sim\mathscr{D}+\{\lambda\overrightarrow{OE'}:\lambda\in[0,1]\}.$$

Proof. Here, we denote by $\boldsymbol{u}_1$ and $\boldsymbol{u}_2$ the vectors given by two edges of $\mathscr{D}$ (different from the $\boldsymbol{u}_1$ and $\boldsymbol{u}_2$ defined in Lemma 2.1). We first show the special case when $\overrightarrow{EE'}\parallel\boldsymbol{u}_1$. Express $\overrightarrow{EE'}=(n+\mu)\boldsymbol{u}_1$ for $n\in\mathbb{Z}$, $0\leq\mu<1$. When $n=0$, we consider the triangular prism $\triangle OEE'+\{\lambda\boldsymbol{u}_2:0\leq\lambda\leq1\}$ (Fig. 3 (a)). Translating it by $\boldsymbol{u}_1$, we obtain, according to Definition 2.1,

$$\triangle OEE'+\{\lambda\boldsymbol{u}_2:0\leq\lambda\leq1\}\sim\triangle OEE'+\{\boldsymbol{u}_1+\lambda\boldsymbol{u}_2:0\leq\lambda\leq1\}.$$

It also holds if we take $\mu=1$. As a result, applying Definition 2.2, we arrive at

$$\mathscr{D}+\{\lambda\overrightarrow{OE}:\lambda\in[0,1]\}\sim\mathscr{D}+\{\lambda\mu\boldsymbol{u}_1+\lambda\overrightarrow{OE}:\lambda\in[0,1]\},\quad 0\leq\mu\leq1.$$

Here, each μ corresponds to a point E' on the edge EF. Thus, it holds that

$$\mathscr{D}+\{\lambda\overrightarrow{OE}:\lambda\in[0,1]\}\sim\mathscr{D}+\{\lambda\overrightarrow{OE'}:\lambda\in[0,1]\}.$$

When $n\neq0$, we could further repeat the above for another n steps.

For general cases, use the point E'' so that $\overrightarrow{EE''}\parallel\boldsymbol{u}_1$ and $\overrightarrow{E''E'}\parallel\boldsymbol{u}_2$. $\square$

Now let us assume that the plane $x=L_2$ contains a lattice point P of the bulk phase. By the above lemma, we have

$$\mathscr{D}\times[0,L_2]\sim\mathscr{D}+\{\lambda\overrightarrow{OP}:0\leq\lambda\leq1\}.$$

Thus, we could turn to the latter parallelepiped.

Let us consider a special case, that is, $\overrightarrow{OP}=\boldsymbol{w}_1$. It means that the plane $x=L_2$ can be written as $a(s_1-1)+bs_2+cs_3=0$. To deal with this case, we specifically choose $\mathscr{D}$ generated by $\boldsymbol{u}_1=b\boldsymbol{w}_1-a\boldsymbol{w}_2$ and $\boldsymbol{u}_2=c\boldsymbol{w}_1-a\boldsymbol{w}_3$. The other two pairs of planes of the parallelepiped are given by $s_2=0,-a$ and $s_3=0,-a$, respectively.

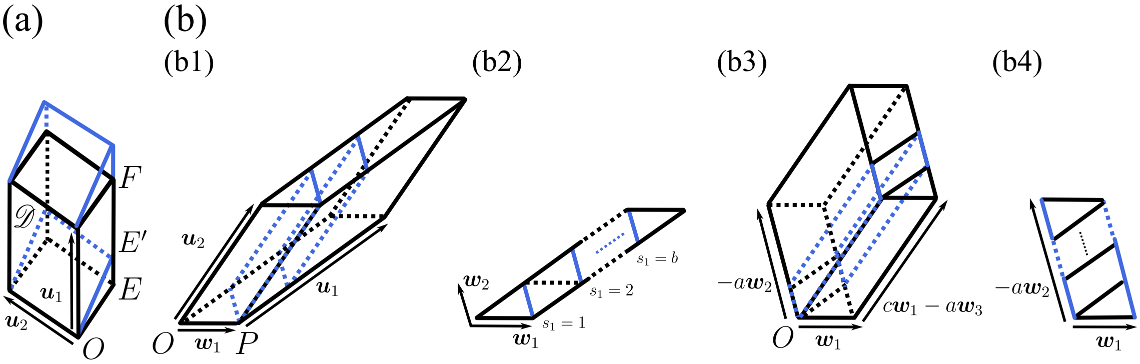

Figure 3: Illustration of Lemma 2.2 and Lemma 2.3. (a) Translating the triangular prism $\triangle OEE'+\{\lambda \boldsymbol{u}_2 : 0\le\lambda\le 1\}$ along u_1 produces an equivalent parallelepiped. (b) Dividing and reassembling parallelepipeds. (b1) Splitting the parallelepiped with the planes $a(s_1-k)+cs_3=0$ (blue dashed parallelograms). (b2) The plane $s_3=0$. (b3) Translating the parallelepiped enclosed by the two blue planes in (b1) by $-k\boldsymbol{w}_1$ gives the reorganized parallelepiped. (b4) The reorganized plane $s_3=0$.

Lemma 2.3. *Let $\mathscr{D}$ be chosen as above. It holds*

$$\mathscr{D}+\{\lambda\boldsymbol{w}_1 : 0\le\lambda\le 1\}\sim\{\lambda_1\boldsymbol{w}_1+\lambda_2(-a\boldsymbol{w}_2)+\lambda_3(-a\boldsymbol{w}_3) : 0\le\lambda_i\le 1\}.$$

Proof. On the plane $s_3=0$ (the base plane of the parallelepiped in Fig. 3 (b1)), let us divide the parallelogram by the lines $s_1=0,\pm1,\cdots,b$, whether taking $+1$ or -1 depends on the sign of b (Fig. 3 (b2)). When translating these lines along $\boldsymbol{u}_2$, the corresponding planes are $a(s_1-k)+cs_3=0$ for $k=0,\cdots,b$ (blue parallelograms in Fig. 3 (b1)), which are parallel. The intersecting lines of one plane and $x=0$ are then written as

$$a(s_1-k)+cs_3=0,\quad as_1+bs_2+cs_3=0.$$

Translating them by $\boldsymbol{w}_1$, we obtain the line

$$a(s_1-k-1)+cs_3=0,\quad a(s_1-1)+bs_2+cs_3=0,$$

which is just the intersecting plane of $a(s_1-k-1)+cs_3=0$ and the plane $x=L_2$. Let $\mathscr{A}_k$ be the part of parallelepiped between two planes $a(s_1-k)+cs_3=0$ and $a(s_1-k-1)+cs_3=0$. (For example, when $k=1$, this corresponds to the parallelepiped between the two blue planes in Fig. 3 (b1).) Let $\mathscr{A}_k$ translate to $\mathscr{A}_k-k\boldsymbol{w}_1$. Since $\boldsymbol{u}_1=b\boldsymbol{w}_1-a\boldsymbol{w}_2$, the blue lines $s_1=k$ in the plane $s_3=0$ collectively form $-a\boldsymbol{w}_2$ after translating each line by $-k\boldsymbol{w}_1$ (Fig. 3 (b4)). Thus, we arrive at

$$\mathscr{D}+\{\lambda\boldsymbol{w}_1 : 0\le\lambda\le 1\}\sim\{\lambda_1\boldsymbol{w}_1+\lambda_2(-a\boldsymbol{w}_2)+\lambda_3(c\boldsymbol{w}_1-a\boldsymbol{w}_3) : 0\le\lambda_i\le 1\}.$$

Carry out similar procedure for the plane $s_2=0$ to obtain the result. □

Theorem 2.1. *Assume that $x=L_2$ contains a lattice point. We can find $\mathscr{A}$ and $\mathscr{B}$ such that $\mathscr{D}\times[0,L_2]=\mathscr{A}\backslash\mathscr{B}$ and $\mathscr{B}\subseteq\mathscr{A}$, such that both $\mathscr{A}$ and $\mathscr{B}$ are equivalent to several whole unit cells.*

Proof. Within the frame $(\boldsymbol{w}_1,\boldsymbol{w}_2,\boldsymbol{w}_3)$, suppose that the point (s_1,s_2,s_3) with $s_i\in\mathbb{Z}$ lies in the plane $x=L_2$. Denote by w_{ix} the x-coordinate of $\boldsymbol{w}_i$ for $i=1,2,3$. Then $\sum_{i=1}^{3} w_{ix}s_i=L_2>0$, meaning that at least some $w_{ix}s_i>0$. We explain the case $w_{1x}s_1,w_{2x}s_2>0$ and $w_{3x}s_3<0$. The other cases can be handled similarly. Consider

$$\mathscr{A}=\mathscr{D}\times[0,w_{1x}s_1+w_{2x}s_2],\quad \mathscr{B}=\mathscr{D}\times(L_2,w_{1x}s_1+w_{2x}s_2].$$

Then $\mathscr{A}\backslash\mathscr{B}=\mathscr{D}\times[0,L_2]$ and $\mathscr{B}\subseteq\mathscr{A}$. Express $\mathscr{A}=\mathscr{A}_1\cup\mathscr{A}_2$, where

$$\mathscr{A}_1=\mathscr{D}\times[0,w_{1x}s_1],\quad \mathscr{A}_2=\mathscr{D}\times[w_{1x}s_1,w_{1x}s_1+w_{2x}s_2].$$

The volume of $\mathscr{A}_1\cap\mathscr{A}_2$ is zero. Since s_i are integers, the planes $x=w_{1x}s_1$ and $x=w_{1x}s_1+w_{2x}s_2$ contain lattice points $(s_1,0,0)$ and $(s_1,s_2,0)$, respectively. By the three lemmas above, $\mathscr{A}_1$ is equivalent to several whole unit cells. After translation, the planes $x=w_{1x}s_1$ and $x=L_2$ pass the origin. Similarly, $\mathscr{A}_2$, and $\mathscr{B}$ are also equivalent to several whole unit cells. □

Numerically, we also need to take care of the finite-size effect by enlarging L_1 and L_2. When doing this, we shall always keep in mind that the boundary planes ought to pass a lattice point.

3 Results and discussions

Now, we shall focus on DG GBs. Specifically, we investigate four GBs with different grain orientations, including the twin boundary reported recently [40]. The coefficients in the energy need to be chosen in the DG region of the phase diagram, which are taken at the values $\tau=-0.4$, $\gamma=0.4$ [58]. The unit cell of DG is a cube, where we recall that the edge length is denoted as a. The orientations and displacements of two grains are specified by their contact plane at $x=0$ (supposing sharp interface, i.e. without relaxation), and further two coincident directions and one coincident point on the plane, as detailed in Table 2. The corresponding rotation matrices are provided in Appendix A.2.

3.1 GB energy

We first look into the computation of GB energy for the four GBs. According to the results in Section 2, both L_1 and L_2 shall pass a lattice point. For the GBs to be examined, the orientations of two grains allow us to take $L_1=L_2=L$ for appropriately chosen L. Then, the GB energy per area, defined in Eq. (2.9), can be simplified as

$$\delta_{\mathrm{GB}}=2L(E(\phi;[-L,L]\times\mathscr{D})-E_0). \tag{3.1}$$

For each GB, we select different lattice points to increase L (that are distinct for these GBs) and plot in Fig. 4 in GB energy obtained from the above formula. It clearly presents the

Table 2: The posing of two grains, where a denotes the edge length of the DG unit cell.

		contact plane	coincident directions		coincident point	GB energy
TB	grain 1	(422)	$[1\bar{1}\bar{1}]$	$[01\bar{1}]$	$(0,0,a/2)$	0.113
	grain 2	(422)	$[\bar{1}11]$	$[0\bar{1}1]$	$(0,0,a/2)$	
NetSw	grain 1	$(\bar{1}\bar{1}\bar{2})$	$[\bar{1}\bar{1}1]$	$[\bar{1}10]$	(0,0,0)	0.098
	grain 2	(112)	$[\bar{1}\bar{1}1]$	$[1\bar{1}0]$	(0,0,0)	
Tlt1	grain 1	$(0\bar{1}\bar{3})$	$[0\bar{3}1]$	$[\bar{1}00]$	(0,0,0)	0.210
	grain 2	$(01\bar{3})$	$[0\bar{3}\bar{1}]$	$[\bar{1}00]$	(0,0,0)	
Tlt2	grain 1	$(\bar{1}\bar{1}\bar{2})$	$[\bar{1}\bar{1}1]$	$[\bar{1}10]$	(0,0,0)	0.273
	grain 2	$(11\bar{2})$	$[\bar{1}\bar{1}\bar{1}]$	$[\bar{1}10]$	(0,0,0)	

(a) TB (b) NetSw

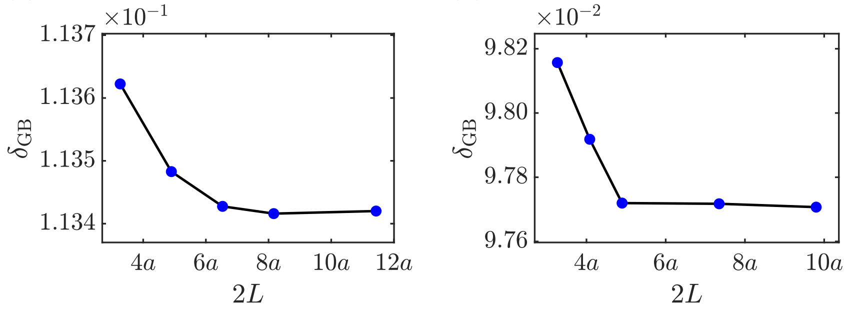

(c) Tlt1 (d) Tlt2

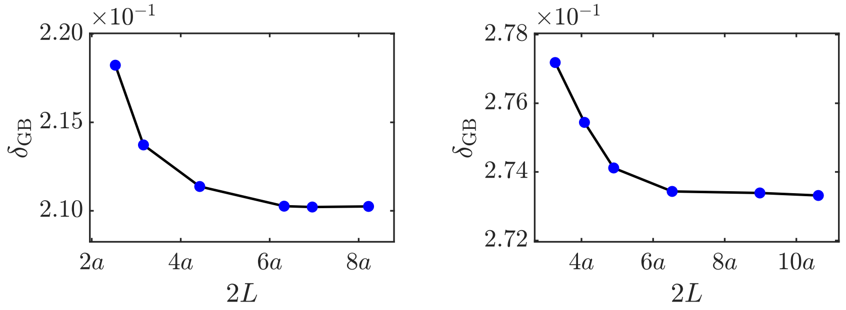

Figure 4: The energy of the four GBs with increasing L. The blue solid points on the curve denote the GB energy when L passes through lattice points.

convergence of GB energy as L increases. When inspecting Eq. (2.9) together with Fig. 1, we notice that choosing L off the lattice points would lead to oscillations at the same magnitude of the GB energy itself. Moreover, the differences of GB energy for TB and NetSw are also no larger than the oscillation in Fig. 1. Therefore, it is significant that the choice of L follows the principle of passing a lattice point, or we cannot identify which GB has lower energy.

Of the four GBs, it turns out that NetSw is the one with the lowest energy, while the two tilt GBs have higher energy. We shall investigate their structures below.

3.2 Network structure

To visualize the skeleton of a GB, we present the isosurface at $\phi=1.6$. Nodes are identified at local maxima whose values are not less than 84% of maximum bulk value. The left-handed and right-handed networks are colored with blue and, respectively.

3.2.1 TB

The skeleton of TB is shown in Fig. 5, with two viewing directions relative to two grains displayed. We affirm the mirror symmetry of TB after verifying that $|\phi(x,y,z)-\phi(-x,y,z)|<10^{-10}$. Comparing the (422) slice of grain 1 and $x=0$ slice of TB (Fig. 5 (b)), we could see that Type-1 to Type-3 nodes are formed exactly in the way claimed in Ref. [40]. We label the nodes with numbers, and use the same number to represent equivalent sites in different unit cells. The new nodes generated on $x=0$ in TB are numbered with 1, 2, 3, where node 1 has four edges and node 2, 3 both have three edges. Notably, node 3 connects only to nodes on $x=0$ (two node 1 and one node 2, see (e1)), whereas node 1 and node 2 connect to two nodes outside $x=0$. When TB nodes are not involved, the network topology of TB is identical to that of bulk DG. Circuits involving TB nodes are divided into category I if nodes in the two grains are connected by TB nodes, and category II if circuits in two grains only share TB nodes (see Fig. 5 (c)). We further specify the number of TB nodes and bulk nodes in the circuits. For instance, I-4,3,3^8 comprises one node 1, one node 2, and eight bulk nodes, while circuit II-4,3^2,3^2,3^4 consists of a single node 1, two node 3, two node 2 and four bulk nodes. The network topology is consistent with that given in Ref. [40].

Substantial deformations occur when three TB nodes are involved. Notably, struts attached to node 1 are elongated over 20% from $0.35a$ (Fig. 5 (c)), and vertical planes appear (Fig. 5 (d1)). The chirality of network is locally reversed as indicated by the dihedral angles (Fig. 5, (d2) and (d4)). However, the values of dihedral angles are surprisingly close to 70.5°, which is different from what is reported previously [40]. Large deviations of strut angles involving node 1 are also observed (Fig. 5 (e1)-(e3)).

In bulk DG, a node and its three adjacent nodes are coplanar. This seems to be well kept in TB when only one node on $x=0$ is involved, as the dihedral angles 8-(1,7)-9 and 9-(2,5)-12 almost equal 180° (Fig. 5, (d4) and (d5), the sum of two adjacent dihedral angles).

Looking into the geometry, we notice that the deviations of strut lengths and dihedral angles are larger than those of strut angles (see Fig. 5, (c), (d6)-(d9) and (e5)-(e8)). Deformations are generally larger when nodes connected to $x=0$ are involved, for example node 4 and 6 (Fig. 5, (c), (d6)-(d7), (e5)-(e6)), particularly in the elongation of struts (6-11

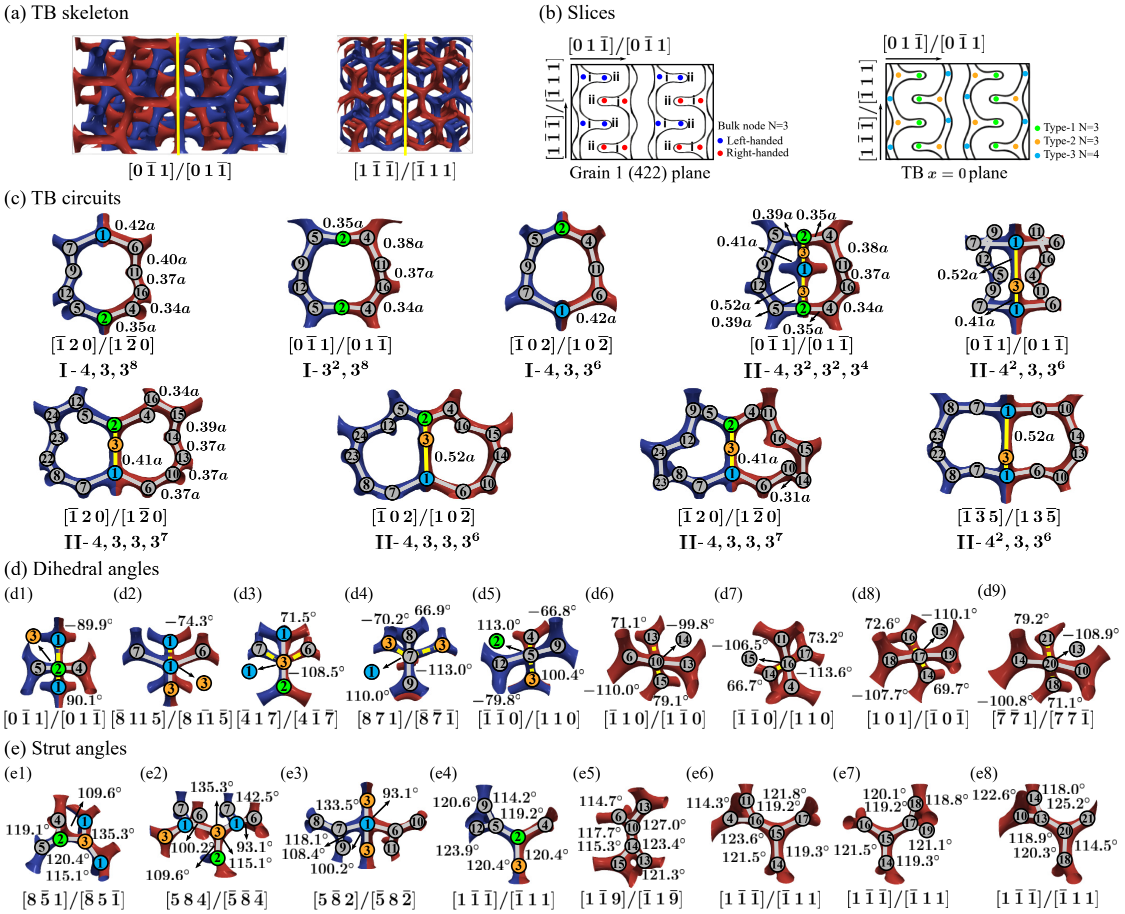

Figure 5: The TB skeletons. The viewing direction with respect to the left/right grain is labeled below each figure. (a) The whole skeletons. (b) The (422) slice in grain 1, the $x=0$ plane in TB, and the nodes. (c) Nine circuits. Nodes with whole periods differences are labeled the same. (d) Dihedral angles, viewing along a strut direction. Solid lines are closer, dashed lines farther. (e) Strut angles.

of the length $0.40a$) and deflection of coplanarity (see dihedral angles 4-(15,16)-11 and 6-(10,14)-13). In contrast, for nodes not connected to $x=0$, coplanarity is almost maintained (for instance, see dihedral angles 13-(14,10)-15, 14-(15,16)-17, 18-(15,17)-19 and 18-(13,20)-21 in Fig. 5 (d6)-(d9)), with a few exceptions (an example is 10-(13,20)-14 in Fig. 5 (d9)). Later, we shall analyze the statistics on changes of strut lengths, strut angles, dihedral angles and coplanarity.

3.2.2 NetSw

The posing of two grains in NetSw suggests that it has a 180° rotational symmetry around the $[\bar{1}\bar{1}1]$ axis of both grains (the y-axis in the computation). Indeed, we confirm it by

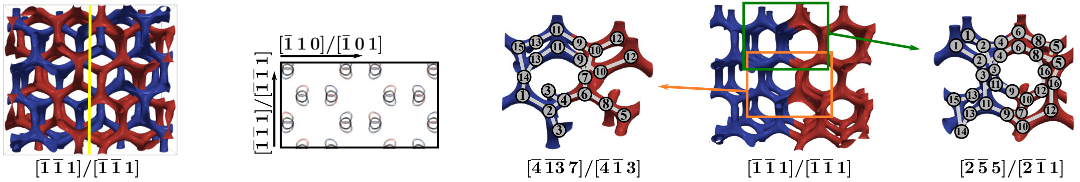
(a) NetSw skeleton (b) Slices (c) One branch network

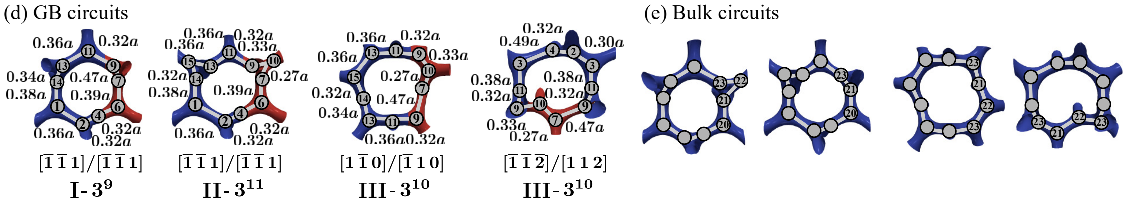
(d) GB circuits (e) Bulk circuits

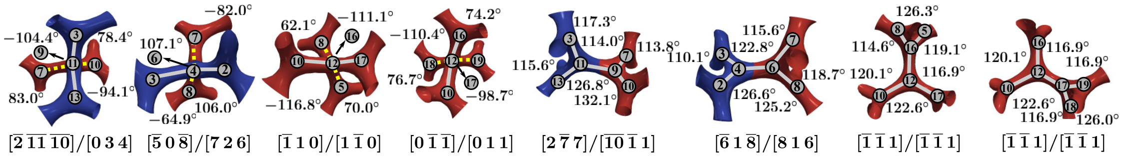
(f) Dihedral angles (g) Strut angles

Figure 6: (a) The NetSw skeleton. (b) Slices of GB (black), grain 1 (blue) and 2 (red) on the plane $x=0$. (c) One branch of the network. (d) Circuits in GB and strut lengths, in comparison with (e) Bulk circuits of grain 1. (f)(g) Dihedral angles and strut angles.

verifying that $|\phi(x,y,z)-\phi(-x,y,-z)|<7\times 10^{-5}$. The skeleton of NetSw is shown in Fig. 6 (a). The networks with different chirality are connected through struts at the plane $x=0$ without generating new nodes, reflected by the slices of two grains before relaxation (Fig. 6 (b), blue and red) and GB (black). Due to the symmetry, we focus on one branch (left blue, right red, Fig. 6 (c)), where we shall remember that the different nodes may share the same number if they are whole periods different. The circuits passing $x=0$ are formed by combining part of left- and right-handed ones, including nine, ten and eleven nodes (Fig. 6 (d)). These circuits have more blue nodes, each of which has a counterpart with more red nodes (Appendix 12). To comprehend these circuits, we compare them with the bulk circuits of grain 1 (6 (e)). It is observed that red nodes 6 and 9 are close to blue nodes 20 and 23 in the bulk, respectively. But the connection between node 6 and 9 is altered due to reverse chirality, resulting in circuits with different lengths. It also causes significant skeleton distortions. While the struts crossing $x=0$ (4-6 and 9-11) deviate less than 10% from $0.35a$, we observe huge elongations (3-4, 7-9) and shrinkages (7-10) in the vicinity of $x=0$. The alterations in dihedral angles (Fig. 6 (f)) and strut angles (Fig. 6 (g)) are also larger near $x=0$, while strut angles generally deviate less than dihedral angles. Meanwhile, by checking the sum of adjacent dihedral angles, we notice that the deflection of coplanarity appears to be much less than the change of dihedral and strut angles. This observation is similar to TB, which we shall revisit later.

3.2.3 Tlt1

The skeleton of Tlt1 is presented in Fig. 7 (a). For both grains, the $[\bar{1}00]$ direction coincides with the z-axis, and the period length in the y-direction is $\sqrt{10}a$ (the height of the orange box in Fig. 7 (a)). We particularly focus on the green box where new node and curved edges appear, drawn in detail in Fig. 7 (b). In Tlt1, networks of the same chirality for both grains are connected. The nodes in the blue and red networks are numbered independently.

We find one new node (number 1) and several curved edges between nodes (green ones in Fig. 7 (b)), which resemble the so-called 'network breaks' topological defects [17]

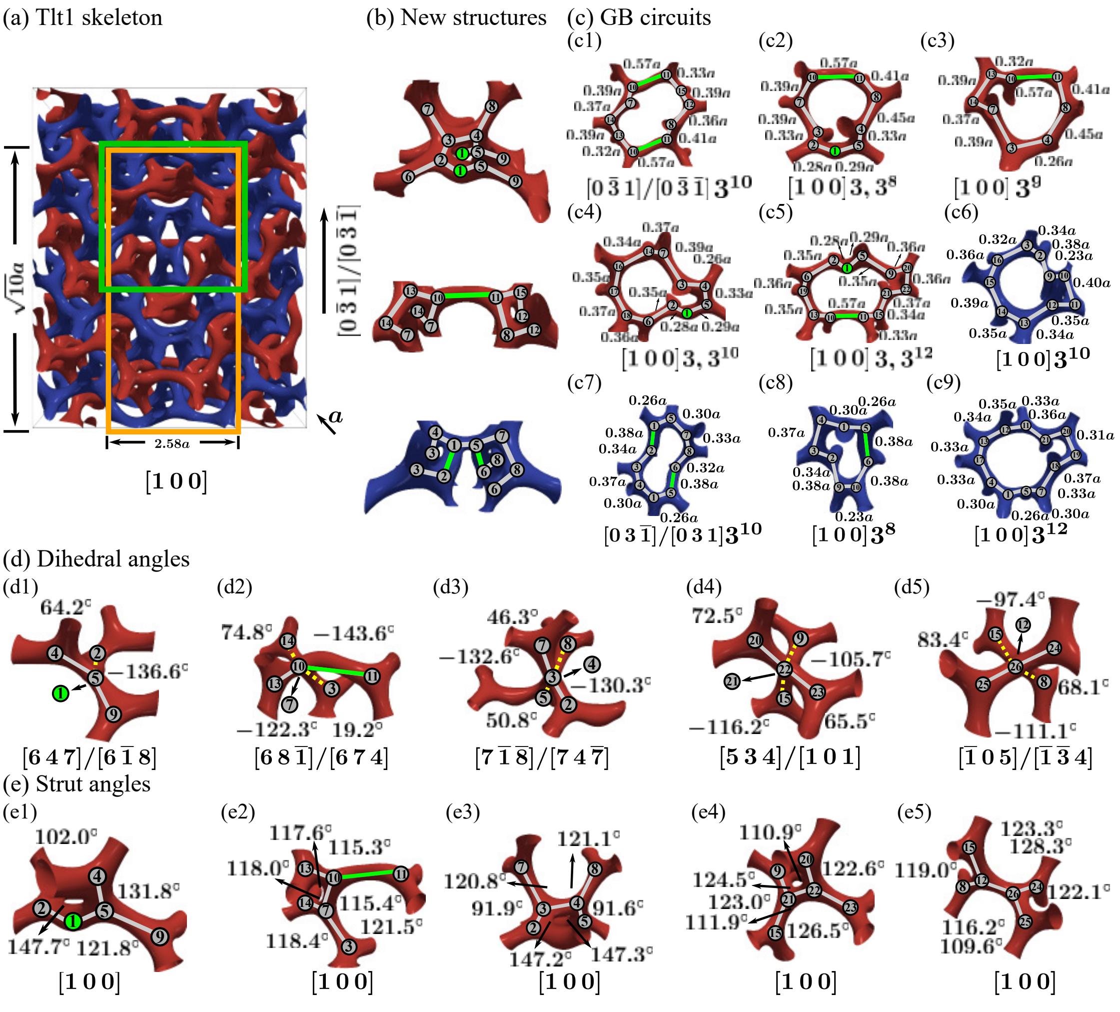

Figure 7: (a) Tlt1 skeleton. The orange box encloses one period. (b) One new GB node and three curved struts. (c)(d)(e) Circuits, dihedral angles and strut angles.

or 'point defects' [33]. The other nodes can be regarded as displaced from bulk nodes, forming circuits crossing $x=0$ (Fig. 7 (c)) in the red network by combining part of left and right grains at node 1, edge 3-4 and 10-11, and in the blue network at edges 1-5, 9-10, and 11-12. Strut lengths in the red network involving nodes (1, 3, 4, 10, 11) and in the blue network involving nodes (1, 5, 9, 10), both connecting two grains, deviate larger than others relative to bulk strut length. The dihedral angles and strut angles clearly vary more drastically than TB and NetSw (Fig. 7, (d) and (e)), even far away from $x=0$ (Fig. 7 (d4), (d5), (e4), (e5)). However, we notice that for many nodes not concerning node 1 and curved edges, coplanarity is almost maintained, such as 2-(3,4)-7, 5-(3,4)-8, 20-(21,22)-23 and 24-(12,26)-25.

3.2.4 Tlt2

The Tlt2 has a skeleton more complicated, for which we present the topology in Fig. 8 (a). Tlt2 is formed by the connection of two grains with identical chirality network at $x=0$. The period in the y-z plane is $\sqrt{3}a\times\sqrt{2}a$. Three new nodes and five curved edges emerge within an orange box spanning approximately 2.68a in the x-direction, as shown in Fig. 8 (b). The nodes in the blue and red networks are numbered independently. To understand these new nodes, we compare them to the corresponding bulk networks of

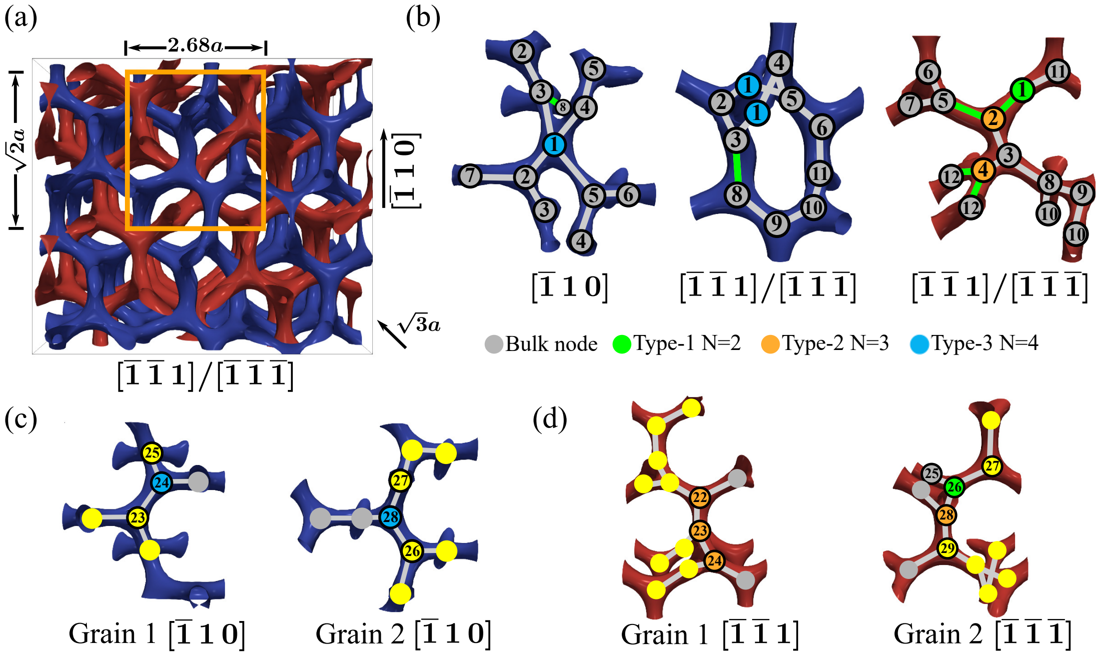

Figure 8: (a) Tlt2 skeleton. The orange box spans one period in the y-direction. (b) Three new nodes marked with different colored dots and five curved struts marked with green lines. (c)-(d) The corresponding bulk networks of two grains neighboring new nodes in (b). The yellow nodes in two grains correspond to the gray nodes in (b).

two grains (Fig. 8 (c)-(d)). In the left-handed network, node 1 with four edges (Type-3) results from the fusion of nodes 24 and 28, each with two edges. Similarly, in the right-handed network, node 2 also emerges as a merging of two bulk DG nodes from two grains (node 22 and 28). Node 4 with three edges (Type-2) is formed by the fusion of two bulk DG nodes of grain 1 (node 23 and 24). Moreover, the strut 25-26 of grain 2 is truncated, forming a new node with two edges (Type-1). In Tlt2, there are also twenty-four GB circuits that differ from the bulk circuits (see Appendix Fig. 13).

3.3 Deformation statistics

We investigate the statistics of deviations for four geometric parameters (strut length, strut angle, dihedral angle and coplanarity) within $x \in [-1.58a, 1.58a]$ that covers the range of deformation for the four GBs examined in the current work. Specifically, for the coplanarity of one node and three adjacent nodes, we examine the maximal deviation of dihedral angles formed by three planes, each determined by the node and its two connecting nodes. The nodes are categorized into three regions: region I comprises nodes on the plane $x=0$; region A includes nodes with a strut touching or crossing $x=0$; the remaining nodes reside in region B. Accordingly, a strut is considered to be in region I if either of its nodes is, in region A if either node is in region A but neither is in region I, and in region B otherwise. The angles are categorized similarly.

The maximum deviations for TB, NetSw, Tlt1 and Tlt2 are listed in Table 3, and histograms are presented in Fig. 9. The histogram intervals are chosen approximately at 3%,7% for strut angles (w.r.t. 120°) and coplanarity (w.r.t. 180°), while 7% and 17% for dihedral angles (w.r.t. 70.5°). For strut lengths, the middle interval is selected to span approximately 6% above and below the bulk value of $0.35a$.

Table 3: Maximum variations for strut lengths, dihedral angles, strut angles, coplanarity.

GBs	region	strut length ($0.35a$)	strut angle (120°)	dihedral angle ($\pm 70.5^\circ$)	coplanarity (180°)
TB	I	$\pm 0.20a$	$\pm 27^\circ$	$\pm 43^\circ$	$\pm 79^\circ$
	A	$\pm 0.05a$	$\pm 9^\circ$	$\pm 17^\circ$	$\pm 13^\circ$
	B	$\pm 0.05a$	$\pm 8^\circ$	$\pm 11^\circ$	$\pm 6^\circ$
NetSw	A	$\pm 0.14a$	$\pm 12^\circ$	$\pm 18^\circ$	$\pm 11^\circ$
	B	$\pm 0.08a$	$\pm 10^\circ$	$\pm 13^\circ$	$\pm 9^\circ$
Tlt1	A	$\pm 0.22a$	$\pm 28^\circ$	$\pm 53^\circ$	$\pm 38^\circ$
	B	$\pm 0.05a$	$\pm 17^\circ$	$\pm 20^\circ$	$\pm 25^\circ$
Tlt2	I	$\pm 0.17a$	$\pm 40^\circ$	$\pm 102^\circ$	$\pm 84^\circ$
	A	$\pm 0.23a$	$\pm 25^\circ$	$\pm 106^\circ$	$\pm 29^\circ$
	B	$\pm 0.09a$	$\pm 16^\circ$	$\pm 12^\circ$	$\pm 14^\circ$

(a) TB

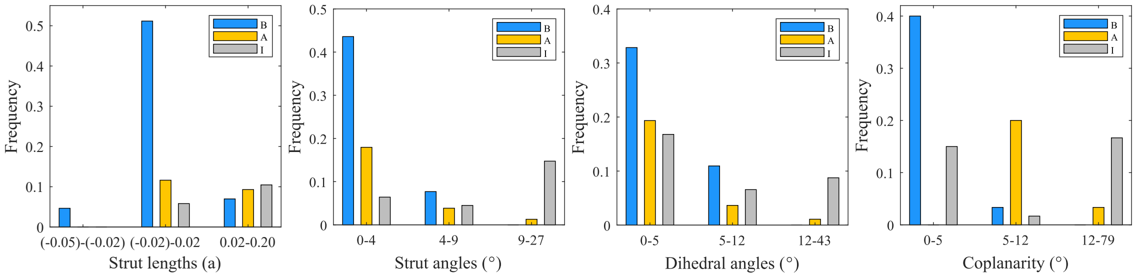

(b) NetSw

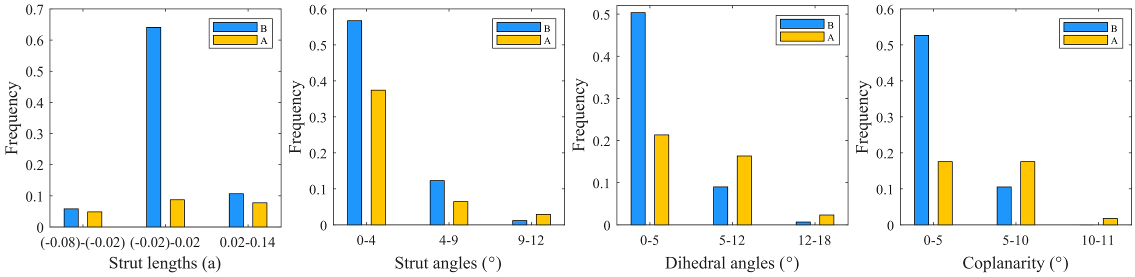

(c) Tlt1

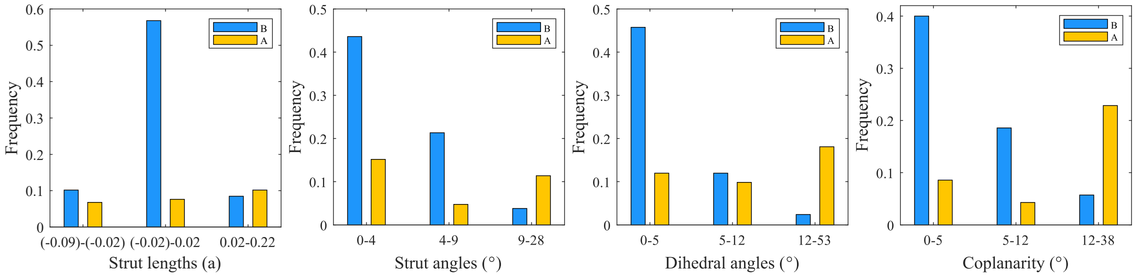

(d) Tlt2

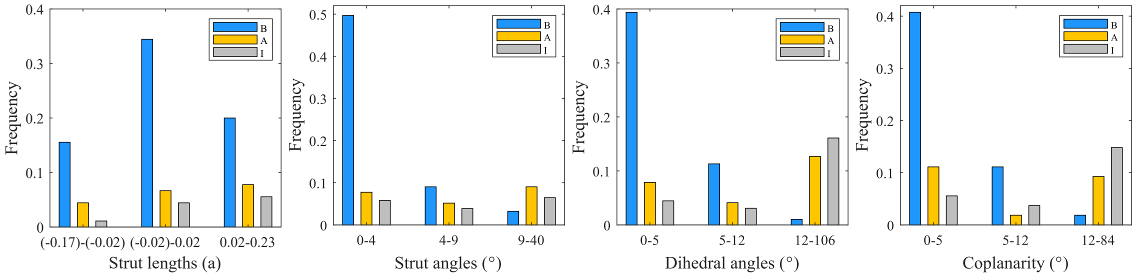

Figure 9: Statistics of deviations for strut lengths, strut angles, dihedral angles and coplanarity.

The statistics clearly indicate that Tlt1 and Tlt2 deform greater than TB and NetSw in all four aspects, potentially contributing to its higher GB energy. Focusing on TB and NetSw, it is evident that huge distortions in TB mostly occur in region I, while the distortions in region A and B might be slightly less than NetSw. It suggests that region I contributes significantly on higher GB energy of TB than NetSw. Furthermore, we are also interested in the comparison of four geometric parameters in region A and B of TB and NetSw. It is noticed that strut lengths and dihedral angles are more prone to altering (many exceeding 7%) than strut angles and coplanarity (most within 7%). In particular, dihedral angles appear to change the most but coplanarity is maintained better, which is consistent with our intuitions obtained from Fig. 5-Fig. 7. This observation implies that coplanarity may play an essential role in GB energy.

3.4 Spectral configurations

Since the GB profile ϕ is periodic in the y-z plane, we could examine its spectral intensities (i.e. moduli of Fourier coefficients, denoted by $|\hat{\phi}(x,\boldsymbol{k})|$ for certain index $\boldsymbol{k}=(k_y,k_z)^T$) as functions of x. Each spectrum is the projection of multiple bulk GB spectra onto the y-z plane. Thus, it is natural to focus on the projection of major bulk indices, i.e. the two classes $\{211\}$ and $\{220\}$. In particular, we investigate those spectra with maximum intensity within $x\in[-L,L]$ exceeding 0.09, which is approximately $36\%(80\%)$ of the intensity of $\{211\}(\{220\})$ in the bulk DG. For the GBs studied in this work, other spectra have the intensities sufficiently smaller. The intensities of the chosen spectra are plotted in Fig. 10, where for TB and NetSw, only the positive x is presented due to mirror symmetry with respect to $x=0$ (but it is not the case for Tlt1 and Tlt2). Furthermore, intensities of different spectra may coincide, so that one curve may represent multiple spectra. The correspondence between the 2D indices $(k_a,k_b)^T$ in GB and the projected 3D indices $(k_1,k_2,k_3)^T$ in bulk DG is also given (dependent on the orientations of grains) in Fig. 10. Their relationship is summarized in Table 4, for which we provide the derivation for TB as an example in Appendix Section A.2.

Let us first look into the spectral indices. The number of chosen spectra (with maximum intensity exceeding 0.09) is 16, 15, 19 and 17 for TB, NetSw, Tlt1 and Tlt2, respectively, of which NetSw is the smallest. Specifically, for TB and NetSw, only projections of major bulk spectra are present. Interestingly, in NetSw, these projections occupy fewer sites in the y-z plane, which may lead to lower GB energy. Conversely, several additional spectra emerge for Tlt1 and Tlt2, which may be closely related to higher GB energy.

To have a closer inspection of the spectral intensities, we compare with the bulk spectral intensities in the y-z plane, defined as follows. Consider two grains (with prescribed

Table 4: The relationship between GB's and DG's spectral indices.

	k_y	k_z
TB	$k_a-k_b=k_1+k_2-k_3$	$k_a=-k_1-k_3$
NetSw	$k_a+k_b=k_1+k_2-k_3$	$k_b=k_1-k_2$
Tlt1	$k_a=-3k_2-k_3$	$k_b=-k_1$
Tlt2	$k_a-k_b=-k_1-k_2-k_3$	$k_b=-k_1+k_2$

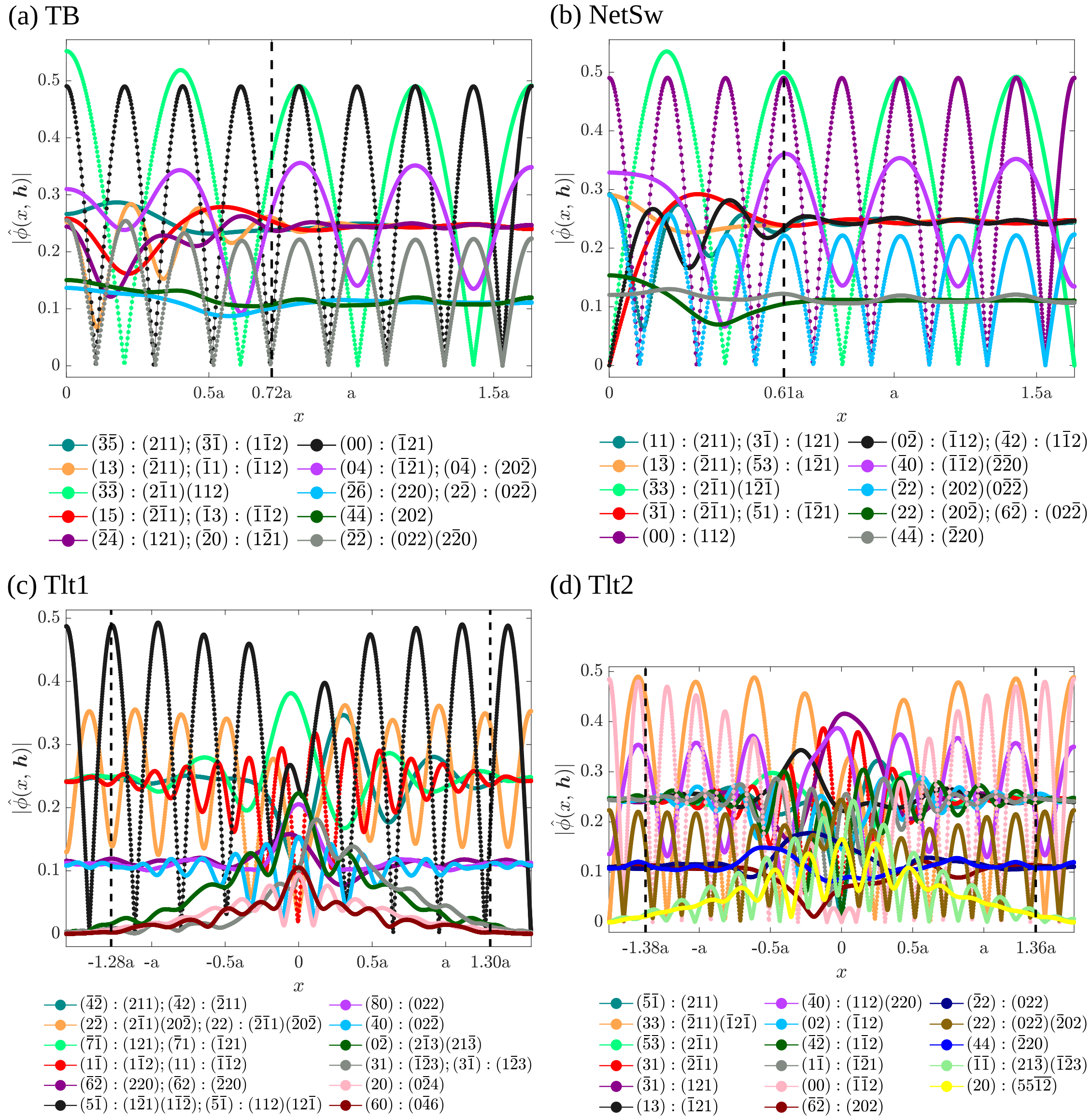

Figure 10: Intensities of spectra against x, for those maximum over 0.09. (a) TB, (b) NetSw, (c) Tlt1 and (d) Tlt2. The black dotted line represents the evaluated boundary of GBs using Eq. (3.2) with $\alpha = 0.03$. The correspondence of bulk indices and 2D projection indices is provided in the legends, where we only list bulk indices with higher intensities in the bulk DG profile.

orientations and displacements) occupying the two half planes $x<0$ and $x>0$. Since they are also periodic in the y-z plane, we can obtain the spectral intensities, denoted as $|\hat{\phi}_{\text{bulk}}(x,\boldsymbol{k})|$. The GB spectral intensities $|\hat{\phi}(x,\boldsymbol{k})|$ resemble $|\hat{\phi}_{\text{bulk}}(x,\boldsymbol{k})|$ when $|x|$ is large, and are distinct near $x=0$. By calculating their difference, we could evaluate the GB width, which is defined as the interval where it exceeds a certain value,

$$\Big| \big|\hat{\phi}(x,\boldsymbol{k})\big| - \big|\hat{\phi}_{\text{bulk}}(x,\boldsymbol{k})\big| \Big| > \alpha \max \big|\hat{\phi}_{\text{bulk}}(x,\boldsymbol{k})\big|. \tag{3.2}$$

To unify the standard, we take $\alpha = 0.03$ for all four GBs. Their widths are $1.44a$, $1.22a$, $2.58a$, $2.74a$ for TB, NetSw, Tlt1, Tlt2, respectively. Indeed, the order of GB width is consistent with that of GB energy.

4 Conclusions

We propose a method of computing GB energy for periodic phases consistent for different grain orientations. The two grains are posed in two halfspaces divided by a plane, applying Fourier expansion along the plane and finite-size truncation in the vertical direction with suitable boundary conditions. The key aspect of consistent GB energy evaluation is that the length of the computational domain is carefully chosen such that each boundary passes a lattice point of the rotated grain, which enables us to conveniently utilize the bulk energy of a unit cell. The results indicate that such a choosing principle is crucial for reliable energy evaluations as it eliminates oscillations at the same magnitude of energy differences between GBs.

We use the method to investigate four double-gyroid GBs. The mirror symmetry of TB, which is proposed in the minimal surface model [38, 39] and roughly seen in experiments [40], is affirmed, while the dihedral angles near TB, despite may reverse the chirality, are closer to 70.5° than experimental results [40]. Despite TB is believed to have low GB energy due to its symmetry, we have found another GB, NetSw, having lower GB energy than TB. Although NetSw does not have mirror symmetry, it has no new nodes and the two networks with reversed chirality are connected directly through struts. By examining the geometric parameters describing the deformations of network, it suggests that coplanarity may be a factor more important on GB energy. This is evidenced by violations of coplanarity in TB due to the formation of new nodes, and larger deviation of coplanarity in Tlt1 and Tlt2. Furthermore, inspection of spectral intensities indicates that the number of high-intensity spectra may also affect the GB energy. It would be of interests to explore whether these observations are also suitable for other DG GBs.

Acknowledgments

This work is supported by the Strategic Priority Research Program of the Chinese Academy of Sciences (No. XDB0510201), National Key R&D Program of China (No. 2023YFA1008802), the National Natural Science Foundation of China (Nos. 12171412, 12288201, 12371414), Beijing Natural Science Foundation (No. JQ25002), the Science and Technology Innovation Program of Hunan Province (No. 2024RC1052), the Innovative Research Group Project of Natural Science Foundation of Hunan Province of China

(No. 2024JJ1008), and the Postgraduate Scientific Research Innovation Project of Hunan Province (No. CX20240589). The computations are done on the High Performance Computing Platform of Xiangtan University.

Appendix

A.1 Bulk DG

In the ideal DG skeleton (illustrated in Fig. 11), each node has three coplanar struts of the length $(\sqrt{2}a)/4 \approx 0.35a$ with a denoting the size of a cubic unit cell. For three consecutive struts (Fig. 11 (b)) whose unit vectors are r_α, r_β, r_γ, respectively, the dihedral angle is defined as that of two half planes containing (r_α, r_β) and (r_β, r_γ), respectively, or equivalently the angle between the two normal vectors $n_{\alpha\beta} = (r_\alpha \times r_\beta)/|r_\alpha \times r_\beta|$ and $n_{\beta\gamma} = (r_\beta \times r_\gamma)/|r_\beta \times r_\gamma|$. The dihedral angles of an ideal DG are $\pm 70.5°$ or $\mp 109.5°$, where "+" ("-") indicates clockwise (counterclockwise).

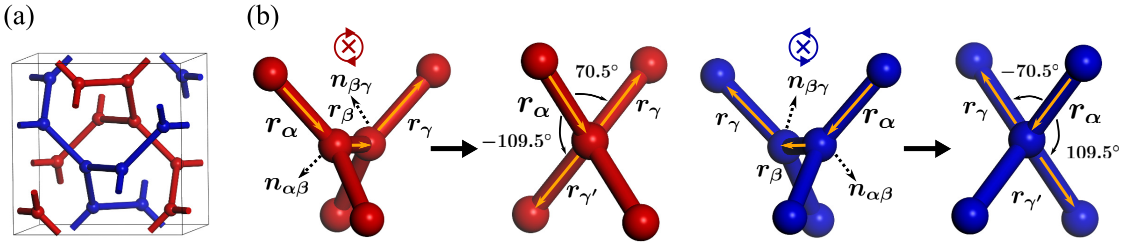

Figure 11: (a) The DG skeleton in a unit cell. (b) Dihedral angles in the two networks with different chiralities.

A.2 Relationship of spectral indices between bulk and GB

For the four GBs examined in this work, listed below are the rotation matrices R_1, R_2 (see Eq. (2.4) of Section 2) of two grains, and the matrices $\tilde{\mathcal{P}}$ for the y-z Fourier expansions. For TB,

$$R_1 = \begin{pmatrix} \frac{1}{\sqrt{6}} & -\frac{1}{\sqrt{3}} & -\frac{1}{\sqrt{2}} \\ -\frac{2}{\sqrt{6}} & -\frac{1}{\sqrt{3}} & 0 \\ -\frac{1}{\sqrt{6}} & \frac{1}{\sqrt{3}} & -\frac{1}{\sqrt{2}} \end{pmatrix}, \quad R_2 = \begin{pmatrix} \frac{1}{\sqrt{6}} & \frac{1}{\sqrt{3}} & \frac{1}{\sqrt{2}} \\ -\frac{2}{\sqrt{6}} & \frac{1}{\sqrt{3}} & 0 \\ -\frac{1}{\sqrt{6}} & -\frac{1}{\sqrt{3}} & \frac{1}{\sqrt{2}} \end{pmatrix}, \quad \tilde{\mathcal{P}} = \begin{pmatrix} \frac{1}{\sqrt{3}}b & -\frac{1}{\sqrt{3}}b \\ -\frac{1}{\sqrt{2}}b & 0 \end{pmatrix}. \tag{A.1}$$

For NetSw,

$$R_1 = \begin{pmatrix} -\frac{1}{\sqrt{6}} & -\frac{1}{\sqrt{3}} & -\frac{1}{\sqrt{2}} \\ -\frac{1}{\sqrt{6}} & -\frac{1}{\sqrt{3}} & \frac{1}{\sqrt{2}} \\ -\frac{2}{\sqrt{6}} & \frac{1}{\sqrt{3}} & 0 \end{pmatrix}, \quad R_2 = \begin{pmatrix} \frac{1}{\sqrt{6}} & -\frac{1}{\sqrt{3}} & \frac{1}{\sqrt{2}} \\ \frac{1}{\sqrt{6}} & -\frac{1}{\sqrt{3}} & -\frac{1}{\sqrt{2}} \\ \frac{2}{\sqrt{6}} & \frac{1}{\sqrt{3}} & 0 \end{pmatrix}, \quad \tilde{\mathcal{P}} = \begin{pmatrix} -\frac{1}{\sqrt{3}}b & -\frac{1}{\sqrt{3}}b \\ 0 & \frac{1}{\sqrt{2}}b \end{pmatrix}. \tag{A.2}$$

For Tlt1,

$$R_1=\begin{pmatrix} 0 & 0 & -1 \\ -\frac{1}{\sqrt{10}} & -\frac{3}{\sqrt{10}} & 0 \\ -\frac{3}{\sqrt{10}} & \frac{1}{\sqrt{10}} & 0 \end{pmatrix}, \quad R_2=\begin{pmatrix} 0 & 0 & -1 \\ \frac{1}{\sqrt{10}} & -\frac{3}{\sqrt{10}} & 0 \\ -\frac{3}{\sqrt{10}} & -\frac{1}{\sqrt{10}} & 0 \end{pmatrix}, \quad \tilde{\mathcal{P}}=\begin{pmatrix} \frac{1}{\sqrt{10}}b & 0 \\ 0 & \frac{3}{\sqrt{10}}b \end{pmatrix}. \tag{A.3}$$

For Tlt2,

$$R_1=\begin{pmatrix} -\frac{1}{\sqrt{6}} & -\frac{1}{\sqrt{3}} & -\frac{1}{\sqrt{2}} \\ -\frac{1}{\sqrt{6}} & -\frac{1}{\sqrt{3}} & \frac{1}{\sqrt{2}} \\ -\frac{2}{\sqrt{6}} & \frac{1}{\sqrt{3}} & 0 \end{pmatrix}, \quad R_2=\begin{pmatrix} \frac{1}{\sqrt{6}} & -\frac{1}{\sqrt{3}} & -\frac{1}{\sqrt{2}} \\ \frac{1}{\sqrt{6}} & -\frac{1}{\sqrt{3}} & \frac{1}{\sqrt{2}} \\ -\frac{2}{\sqrt{6}} & -\frac{1}{\sqrt{3}} & 0 \end{pmatrix}, \quad \tilde{\mathcal{P}}=\begin{pmatrix} \frac{1}{\sqrt{3}}b & -\frac{1}{\sqrt{3}}b \\ 0 & \frac{1}{\sqrt{2}}b \end{pmatrix}. \tag{A.4}$$

The relationship between GB indices and bulk indices can be established using these matrices. For TB, the matrices $\tilde{\mathcal{P}}_s$ of two grains, defined in Section 2, are given by

$$\tilde{\mathcal{P}}_1=\tilde{R}_1^T\mathcal{P}=\begin{pmatrix} -\frac{1}{\sqrt{3}}b & -\frac{1}{\sqrt{3}}b & \frac{1}{\sqrt{3}}b \\ -\frac{1}{\sqrt{2}}b & 0 & -\frac{1}{\sqrt{2}}b \end{pmatrix}, \quad \tilde{\mathcal{P}}_2=\tilde{R}_2^T\mathcal{P}=\begin{pmatrix} \frac{1}{\sqrt{3}}b & \frac{1}{\sqrt{3}}b & -\frac{1}{\sqrt{3}}b \\ \frac{1}{\sqrt{2}}b & 0 & \frac{1}{\sqrt{2}}b \end{pmatrix}. \tag{A.5}$$

For 2D index $\boldsymbol{k}'=(k_a,k_b)^T\in\mathbb{Z}^2$, the spectrum vector $(k_y,k_z)^T$ of TB is

$$\tilde{\mathcal{P}}\boldsymbol{k}'=\begin{pmatrix} \frac{1}{\sqrt{3}}b(k_a-k_b) \\ -\frac{1}{\sqrt{2}}bk_a \end{pmatrix}. \tag{A.6}$$

For 3D index $\boldsymbol{k}''=(k_1,k_2,k_3)^T\in\mathbb{Z}^3$, the spectrum vector $(k_y,k_z)^T$ of grain 2 is

$$\tilde{\mathcal{P}}_2\boldsymbol{k}''=\begin{pmatrix} \frac{1}{\sqrt{3}}b(k_1+k_2-k_3) \\ \frac{1}{\sqrt{2}}b(k_1+k_3) \end{pmatrix}. \tag{A.7}$$

Then we can obtain the relationship between TB and bulk grain 2 (see Table 4). For other GBs, the procedure is similar.

A.3 Further information on GB structures

A.3.1 NetSw

The four circuits passing $x=0$ with more red nodes are presented in Fig. 12. Still, we compare these circuits with bulk circuits of grain 2. It is observed that the positions of blue nodes 11 and 4 are close to red nodes 24 and 25 in the bulk, respectively, with connections distinct from the bulk. This generates circuits of different lengths.

A.3.2 Tlt2

Tlt2 circuits crossing $x=0$ (Fig. 13) are formed in the blue network by combining parts of grain 1 and grain 2 at edges 1-4, 1-5, 8-9, and in the red network at edge 2-3. In the blue network, strut lengths involving nodes 1, 4, 5, 8, 9 connecting two grains, as well as in the red network involving nodes 1, 2, 3, deviate larger than others.

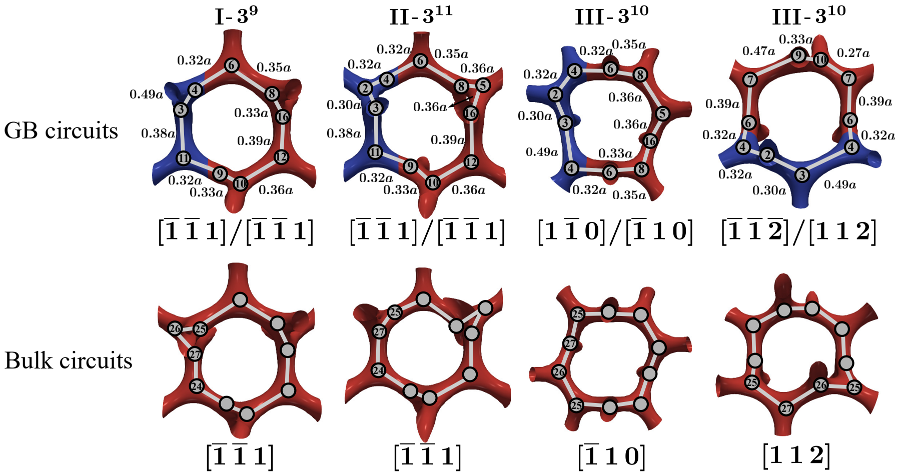

Figure 12: The circuits in NetSw and their corresponding bulk circuits in grain 2.

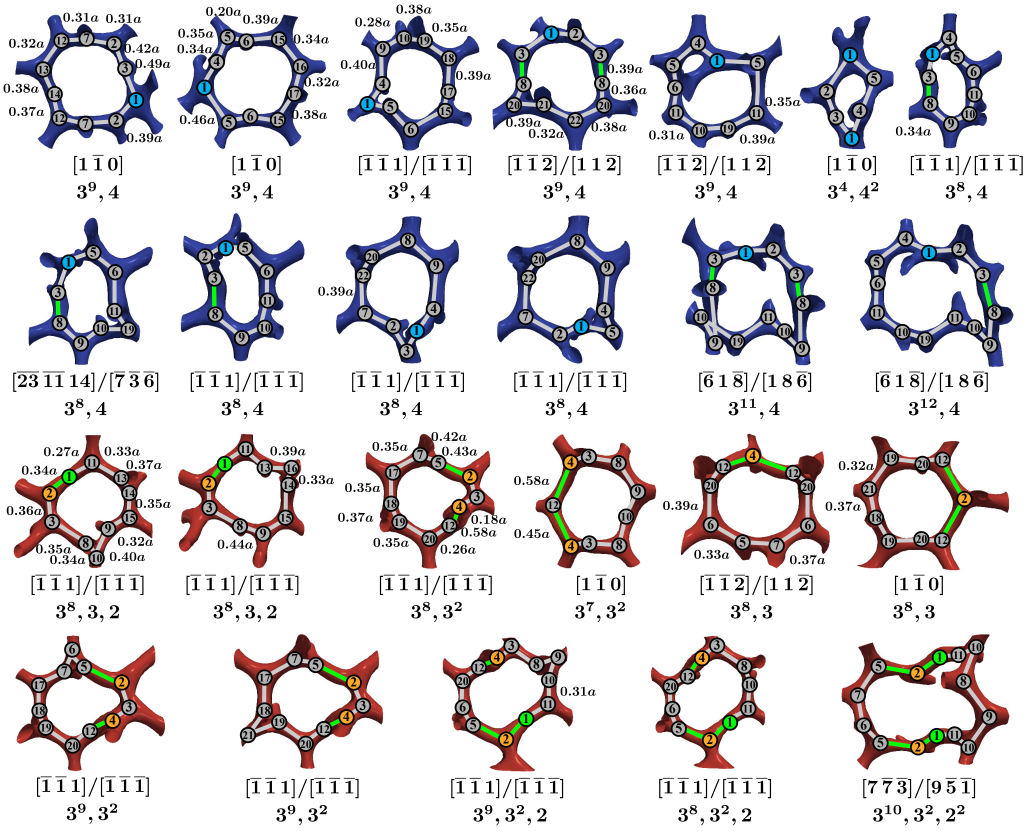

Figure 13: Circuits in Tlt2.

References

[1] Raghunath Roy, Jong Keun Park, Wen-Shiue Young, Sarah E Mastroianni, Maëva S Tureau, and Thomas H Epps III. Double-gyroid network morphology in tapered diblock copolymers. *Macromolecules*, 44(10):3910–3915, 2011.

[2] Damian A. Hajduk, Paul E. Harper, Sol M. Gruner, Christian C. Honeker, Gia Kim, Edwin L. Thomas, and Lewis J. Fetters. The gyroid: A new equilibrium morphology in weakly segregated diblock copolymers. *Macromolecules*, 27(15):4063–4075, 1994.

[3] Adam J Meuler, Marc A Hillmyer, and Frank S Bates. Ordered network mesostructures in block polymer materials. *Macromolecules*, 42(19):7221–7250, 2009.

[4] Jinseok Park and Karen I. Winey. Double gyroid morphologies in precise ion-containing multiblock copolymers synthesized via step-growth polymerization. *JACS Au*, 2(8):1769–1780, 2022.

[5] Yu Cao, Mohamed Alaasar, Asritha Nallapaneni, Mirosław Salamończyk, Peter Marinko, Ewa Gorecka, Carsten Tschierske, Feng Liu, Nata ša Vaupotič, and Chenhui Zhu. Molecular packing in double gyroid cubic phases revealed via resonant soft X-ray scattering. *Phys. Rev. Lett.*, 125:027801, Jul 2020.

[6] OA Otmakhova, AA Piryazev, GN Bondarenko, GA Shandryuk, AV Maryasevskaya, AS Merekalov, DA Ivanov, and RV Talroze. New complexes of liquid crystal discotic triphenylenes: Induction of the double gyroid phase. *Physical Chemistry Chemical Physics*, 23(31):16827–16836, 2021.

[7] William Longley and Thomas J McIntosh. A bicontinuous tetrahedral structure in a liquid-crystalline lipid. *Nature*, 303(5918):612–614, 1983.

[8] Simone Aleandri and Raffaele Mezzenga. The physics of lipidic mesophase delivery systems. *Physics Today*, 73(7):38–44, 2020.

[9] Michael P Tate, Vikrant N Urade, Steven J Gaik, Christopher P Muzzillo, and Hugh W Hillhouse. How to dip-coat and spin-coat nanoporous double-gyroid silica films with EO_{19}-PO_{43}-EO_{19} surfactant (pluronic P84) and know it using a powder X-ray diffractometer. *Langmuir*, 26(6):4357–4367, 2010.

[10] Gregory P Sorenson and Mahesh K Mahanthappa. Unexpected role of linker position on ammonium gemini surfactant lyotropic gyroid phase stability. *Soft Matter*, 12(8):2408–2415, 2016.

[11] Vikrant N Urade, Ta-Chen Wei, Michael P Tate, Jonathan D Kowalski, and Hugh W Hillhouse. Nanofabrication of double-gyroid thin films. *Chemistry of Materials*, 19(4):768–777, 2007.

[12] Kristel Michielsen and Doekele G Stavenga. Gyroid cuticular structures in butterfly wing scales: Biological photonic crystals. *Journal of The Royal Society Interface*, 5(18):85–94, 2008.

[13] Alexander S Finnemore, Maik RJ Scherer, Richard Langford, Sumeet Mahajan, Sabine Ludwigs, Fiona C Meldrum, and Ullrich Steiner. Nanostructured calcite single crystals with gyroid morphologies. *Advanced Materials*, 21(38-39):3928–3932, 2009.

[14] Vinodkumar Saranathan, Chinedum O Osuji, Simon GJ Mochrie, Heeso Noh, Suresh Narayanan, Alec Sandy, Eric R Dufresne, and Richard O Prum. Structure, function, and self-assembly of single network gyroid (I 4132) photonic crystals in butterfly wing scales. *Proceedings of the National Academy of Sciences*, 107(26):11676–11681, 2010.

[15] Hsiao-Fang Wang, Po-Ting Chiu, Chih-Ying Yang, Zhi-Hong Xie, Yu-Chueh Hung, Jing-Yu Lee, Jing-Cherng Tsai, Ishan Prasad, Hiroshi Jinnai, Edwin L. Thomas, and Rong-Ming Ho. Networks with controlled chirality via self-assembly of chiral triblock terpolymers. *Science*

Advances, 6(42):eabc3644, 2020.

[16] Ishan Prasad, Hiroshi Jinnai, Rong-Ming Ho, Edwin L. Thomas, and Gregory M. Grason. Anatomy of triply-periodic network assemblies: Characterizing skeletal and inter-domain surface geometry of block copolymer gyroids. *Soft Matter*, 14(18):3612–3623, 4 2018.

[17] Xueyan Feng, Hua Guo, and Edwin L. Thomas. Topological defects in tubular network block copolymers. *Polymer*, 168:44–52, 2019.

[18] Benita J. Dair, Christian C. Honeker, David B. Alward, Apostolos Avgeropoulos, Nikos Hadjichristidis, Lewis J. Fetters, Malcolm Capel, and Edwin L. Thomas. Mechanical properties and deformation behavior of the double gyroid phase in unoriented thermoplastic elastomers. *Macromolecules*, 32(24):8145–8152, 1999.

[19] BJ Dair, A Avgeropoulos, N Hadjichristidis, M Capel, and EL Thomas. Oriented double gyroid films via roll casting. *Polymer*, 41(16):6231–6236, 2000.

[20] Lei Yang, Chunze Yan, Haiyang Fan, Zhaoqing Li, Chao Cai, Peng Chen, Yusheng Shi, and Shoufeng Yang. Investigation on the orientation dependence of elastic response in gyroid cellular structures. *Journal of the Mechanical Behavior of Biomedical Materials*, 90:73–85, 2019.

[21] Xing Peng, Qiyuan Huang, Yali Zhang, Xiaogang Zhang, Tongtong Shen, Haoyu Shu, and Zhongmin Jin. Elastic response of anisotropic gyroid cellular structures under compression: Parametric analysis. *Materials & Design*, 205:109706, 2021.

[22] Ramon Miralbes, Saul Higuera, David Ranz, and Jose Antonio Gomez. Comparative analysis of mechanical properties and energy absorption capabilities of functionally graded and non-graded thermoplastic sheet gyroid structures. *Mechanics of Advanced Materials and Structures*, 29(26):5142–5155, 2022.

[23] Rachael Sharp, Matthew H Pelletier, William R Walsh, Cambre N Kelly, and Ken Gall. Corrosion resistance of 3D printed Ti6Al4V gyroid lattices with varying porosity. *Materials*, 15(14):4805, 2022.

[24] Kahyun Hur, Yan Francescato, Vincenzo Giannini, Stefan A. Maier, Richard G. Hennig, and Ulrich Wiesner. Three-dimensionally isotropic negative refractive index materials from block copolymer self-assembled chiral gyroid networks. *Angewandte Chemie International Edition*, 50(50):11985–11989, oct 2011.

[25] James A Dolan, Bodo D Wilts, Silvia Vignolini, Jeremy J Baumberg, Ullrich Steiner, and Timothy D Wilkinson. Optical properties of gyroid structured materials: From photonic crystals to metamaterials. *Advanced Optical Materials*, 3(1):12–32, 2015.

[26] Shuai Ma, Qian Tang, Qixiang Feng, Jun Song, Xiaoxiao Han, and Fuyu Guo. Mechanical behaviours and mass transport properties of bone-mimicking scaffolds consisted of gyroid structures manufactured using selective laser melting. *Journal of the Mechanical Behavior of Biomedical Materials*, 93:158–169, 2019.

[27] FSL Bobbert, K Lietaert, Ali Akbar Eftekhari, Behdad Pouran, SM Ahmadi, Harrie Weinans, and AA Zadpoor. Additively manufactured metallic porous biomaterials based on minimal surfaces: A unique combination of topological, mechanical, and mass transport properties. *Acta Biomaterialia*, 53:572–584, 2017.

[28] A Yánez, A Cuadrado, O Martel, H Afonso, and D Monopoli. Gyroid porous titanium structures: A versatile solution to be used as scaffolds in bone defect reconstruction. *Materials & Design*, 140:21–29, 2018.

[29] Ji-Wang Luo, Li Chen, Ting Min, Feng Shan, Qinjun Kang, and WenQuan Tao. Macroscopic transport properties of gyroid structures based on pore-scale studies: Permeability, diffusivity and thermal conductivity. *International Journal of Heat and Mass Transfer*, 146:118837, 2020.

[30] SN Khaderi, VS Deshpande, and NA Fleck. The stiffness and strength of the gyroid lattice. *International Journal of Solids and Structures*, 51(23-24):3866–3877, 2014.

[31] Hiroshi Jinnai, Takashi Kajihara, Hideyuki Watashiba, Yukihiro Nishikawa, and Richard J Spontak. Interfacial and topological measurements of bicontinuous polymer morphologies. *Physical Review E*, 64(1):010803, 2001.

[32] Zihui Li, Kahyun Hur, Hiroaki Sai, Takeshi Higuchi, Atsushi Takahara, Hiroshi Jinnai, Sol M Gruner, and Ulrich Wiesner. Linking experiment and theory for three-dimensional networked binary metal nanoparticle–triblock terpolymer superstructures. *Nature Communications*, 5(1):3247, 2014.

[33] Tomohiro Miyata, Hsiao-Fang Wang, Takafumi Suenaga, Daisuke Watanabe, Hironori Marubayashi, and Hiroshi Jinnai. Dislocation-induced defect formation in a double-gyroid network. *Macromolecules*, 55(18):8143–8149, 2022.

[34] Wenpeng Shan, Vivek Subramanian, Xueyan Feng, and Edwin L Thomas. The nature of crystallographic defects in noncrystalline tubular network block copolymers. *Giant*, page 100216, 2023.

[35] BJ Dair, A Avgeropoulos, N Hadjichristidis, and EL Thomas. Mechanical properties of the double gyroid phase in oriented thermoplastic elastomers. *Journal of Materials Science*, 35:5207–5213, 2000.

[36] Xueyan Feng, Christopher J Burke, Mujin Zhuo, Hua Guo, Kaiqi Yang, Abhiram Reddy, Ishan Prasad, Rong-Ming Ho, Apostolos Avgeropoulos, Gregory M Grason, et al. Seeing mesoatomic distortions in soft-matter crystals of a double-gyroid block copolymer. *Nature*, 575(7781):175–179, 2019.

[37] Silvia Vignolini, Nataliya A. Yufa, Pedro S. Cunha, Stefan Guldin, Ilia Rushkin, Morgan Stefik, Kahyun Hur, Ulrich Wiesner, Jeremy J. Baumberg, and Ullrich Steiner. A 3D optical metamaterial made by self-assembly. *Advanced Materials*, 24(10):OP23–OP27, oct 2011.

[38] Hao Chen. Minimal twin surfaces. *Experimental Mathematics*, 28(4):404–419, jan 2018.

[39] Lu Han, Nobuhisa Fujita, Hao Chen, Chenyu Jin, Osamu Terasaki, and Shunai Che. Crystal twinning of bicontinuous cubic structures. *IUCrJ*, 7(Pt 2):228—237, March 2020.

[40] Xueyan Feng, Mujin Zhuo, Hua Guo, and Edwin L. Thomas. Visualizing the double-gyroid twin. *Proceedings of the National Academy of Sciences*, 118(12):e2018977118, 2021.

[41] Mark A Tschopp, Shawn P Coleman, and David L McDowell. Symmetric and asymmetric tilt grain boundary structure and energy in Cu and Al (and transferability to other fcc metals). *Integrating Materials and Manufacturing Innovation*, 4:176–189, 2015.

[42] Saiyi Li, Liang Yang, and Chunming Lai. Atomistic simulations of energies for arbitrary grain boundaries. part I: Model and validation. *Computational Materials Science*, 161:330–338, 2019.

[43] Vasily V. Bulatov, Bryan W. Reed, and Mukul Kumar. Grain boundary energy function for fcc metals. *Acta Materialia*, 65:161–175, 2014.

[44] Eric N. Hahn, Saryu J. Fensin, Timothy C. Germann, and Marc André Meyers. Symmetric tilt boundaries in body-centered cubic tantalum. *Scripta Materialia*, 116:108–111, 2016.

[45] Kevin Hult Blixt and Håkan Hallberg. Evaluation of grain boundary energy, structure and stiffness from phase field crystal simulations. *Modelling and Simulation in Materials Science and Engineering*, 30(1):014002, 2021.

[46] Jie Xu, Chu Wang, An-Chang Shi, and Pingwen Zhang. Computing optimal interfacial structure of modulated phases. *Communications in Computational Physics*, 21(1):1–15, 2017.

[47] Duo Cao, Jie Shen, and Jie Xu. Computing interface with quasiperiodicity. *Journal of Computational Physics*, 424:109863, 2021.

[48] Kai Jiang, Wei Si, and Jie Xu. Tilt grain boundaries of hexagonal structures: A spectral viewpoint. *SIAM Journal on Applied Mathematics*, 82(4):1267–1286, 2022.

[49] Sov Brazovskii. Phase transition of an isotropic system to a nonuniform state. *Sov. Phys. JETP*, 41:85, 1975.

[50] Glenn H. Fredrickson and Eugene Helfand. Fluctuation effects in the theory of microphase separation in block copolymers. *The Journal of Chemical Physics*, 87(1):697–705, 1987.

[51] E.I. Kats, V.V. Lebedev, and A.R. Muratov. Weak crystallization theory. *Physics Reports*, 228(1):1–91, 1993.

[52] Pingwen Zhang and Xinwei Zhang. An efficient numerical method of Landau–Brazovskii model. *Journal of Computational Physics*, 227(11):5859–5870, 2008.

[53] Ludwik Leibler. Theory of microphase separation in block copolymers. *Macromolecules*, 13(6):1602–1617, 1980.

[54] Takao Ohta and Kyozi Kawasaki. Equilibrium morphology of block copolymer melts. *Macromolecules*, 19(10):2621–2632, 1986.

[55] Kai Jiang, Wei Si, Chang Chen, and Chenglong Bao. Efficient numerical methods for computing the stationary states of phase field crystal models. *SIAM Journal on Scientific Computing*, 42(6):B1350–B1377, 2020.

[56] Chenglong Bao, Chang Chen, Kai Jiang, and Lingyun Qiu. Convergence analysis for Bregman iterations in minimizing a class of Landau free energy functionals. *SIAM Journal on Numerical Analysis*, 62(1):476–499, 2024.

[57] Xiaomei Yao, Jie Xu, and Lei Zhang. Transition pathways in cylinder-gyroid interface. *Communications in Computational Physics*, 32(3):810–828, 2022.

[58] Duncan McClenagan. *Landau theory of complex ordered phases*. PhD thesis, McMaster University, 2019.